



저작자표시-비영리-변경금지 2.0 대한민국

이용자는 아래의 조건을 따르는 경우에 한하여 자유롭게

- 이 저작물을 복제, 배포, 전송, 전시, 공연 및 방송할 수 있습니다.

다음과 같은 조건을 따라야 합니다:



저작자표시. 귀하는 원저작자를 표시하여야 합니다.



비영리. 귀하는 이 저작물을 영리 목적으로 이용할 수 없습니다.



변경금지. 귀하는 이 저작물을 개작, 변형 또는 가공할 수 없습니다.

- 귀하는, 이 저작물의 재이용이나 배포의 경우, 이 저작물에 적용된 이용허락조건을 명확하게 나타내어야 합니다.
- 저작권자로부터 별도의 허가를 받으면 이러한 조건들은 적용되지 않습니다.

저작권법에 따른 이용자의 권리는 위의 내용에 의하여 영향을 받지 않습니다.

이것은 [이용허락규약\(Legal Code\)](#)을 이해하기 쉽게 요약한 것입니다.

[Disclaimer](#)

이학박사학위논문

**Study of Structural Changes in  
Two-dimensional Materials based  
on Cohesive Energy Analysis**

원자간 결합 에너지 분석에 기초한 이차원  
물질에서의 구조 변화 연구

2018년 2월

서울대학교 대학원  
물리천문학부  
김동욱



# Study of Structural Changes in Two-dimensional Materials based on Cohesive Energy Analysis

원자간 결합 에너지 분석에 기초한 이차원  
물질에서의 구조 변화 연구

양범정 교수님

이 논문을 이학박사 학위논문으로 제출함

2018년 1월

서울대학교 대학원

물리천문학부

김동욱

김동욱의 박사 학위논문을 인준함

2018년 2월

위원장 박철환 (인)

부위원장 양범정 (인)

위원 박윤 (인)

위원 민흥기 (인)

위원 유병덕 (인)



**Study of Structural Changes in  
Two-dimensional Materials based on  
Cohesive Energy Analysis**

**Dongwook Kim**

Supervised by

**Bohm Jung Yang**

A Dissertation

Submitted to the Faculty of

Seoul National University

in Partial Fulfillment of

the Requirements for the Degree of

Doctor of Philosophy

Jan. 2018

Department of Physics and Astronomy

The Graduate School

Seoul National University



# Abstract

## **Study of Structural Changes in Two-dimensional Materials based on Cohesive Energy Analysis**

Dongwook Kim

Department of Physics and Astronomy

The Graduate School

Seoul National University

Periodicity is most important concept in understanding of condensed matter or solid. Two-dimensional material is special due to its constraint periodicity only along two independent directions in three-dimensional space. The most famous 2d material may be graphene, which is exfoliated from graphite by K. S. Novoselov and A. K. Geim in 2004. There have been other monolayer materials except for graphene, for example, transition metal dichalcogenides and h-BN. Their physical properties were also reported in various aspects. They have common properties that they could be forming layered structure through van der Waal interaction between each layers. Due to the weak interlayer binding from vdW-interaction, layered structure could be formed with various physical properties depending on number of layer, stacking, and the kinds of stacked monolayer, which have attracted many

researchers in academic and engineering fields. Reflecting this increasing interest in 2d materials, I considered two subjects constituting my thesis with a tremendous help of calculation using density functional theory.

In first part, I analyzed the structure transformation near GB in polycrystalline graphene and obtaining energy curves corresponding structure transformation processed for quantitative understanding using DFT calculation. I categorized two main structure transformation inducing most of structure transformation observed in TEM experiments. first one is SW-transformation well known in pristine graphene, however the value of energy barrier is reduced than that in pristine graphene, which means the easier occurrence near grain boundary. the other one is evaporation of carbon dimer reducing two carbon atom in the graphene sheet. From the value of energy barrier obtained by DFT calculation, this structure transformation is also much easier to occur near grain boundary than similar structure transformation in pristine graphene with perfect hexagonal structure. From the observation of relaxed structure using DFT calculation, I understood that the energy barrier decrease due to atomic structure reconstruction only possible near grain boundary and the role of TEM imaging in structure transformation of grain boundary in graphene.

in second part, I studied on  $\text{Al}(\text{OH})_3$  with layered structure. Until now the vdW-interaction is usual interlayer binding mechanism in various materials with layered structure. Starting from scrutinizing two bulk phase of  $\text{Al}(\text{OH})_3$  with layered structure, I tried to understand its monolayer structure and their binding with hydrogen bonding as interlayer binding mechanism. Using DFT calculation, I quantitatively find out interlayer binding by hydrogen

bonds is weaker interaction comparing to the strong ionic bonding existed in single layer structure. So, energetically, I could consider  $\text{Al}(\text{OH})_3$  as a layered material, However, it shows stronger binding than the layered structure bound by vdW-interaction. In band structural aspect, I also find out the surface state observed in conduction band bottom region in case of single layer or slab structure (finite number of layers), which is not found in the result for bulk structure. This surface state become a main reason of decreasing band gap of 2d structure necessarily having surface. Finally, I suggest Alkali-halide intercalation as a tailoring method for layered  $\text{Al}(\text{OH})_3$  not only in crystal structure, but also in electronic band structure. Interlayer distance, the most important element in application of layered material, is affected by kinds of Alkali atom and halogen atom at the same time. Electronic band structure, especially in valence band region, also could be engineered by Alkali-halide intercalation, easily understood by hybridization among p-orbitals of halogen and oxygen atoms.

**Keywords :** Two-dimensional material, cohesive energy, total energy, Density functional theory

**Student Number :** 2010-20359



# Contents

<b>Abstract</b> . . . . .	<b>i</b>
<b>I. Introduction</b> . . . . .	<b>1</b>
<b>II. Computational Methods</b> . . . . .	<b>5</b>
2.1 Density Functional Theory . . . . .	5
2.1.1 Hohenberg-Kohn Theorem . . . . .	6
2.1.2 Kohn-Sham equation . . . . .	8
2.1.3 The Approximation of Exchange-correlation Func- tional : LDA and GGA Approximation . . . . .	10
2.2 The plane wave basis sets and Pseudopotential . . . . .	12
2.2.1 Plane wave basis . . . . .	12
2.2.2 Projector augmented waves(PAW) method . . . . .	13
<b>III. Atomic-scale investigation of grain boundary motion in graphene</b>	<b>15</b>
3.1 Introduction . . . . .	15
3.2 Computational Details . . . . .	16
3.3 Result and discussion . . . . .	18
3.3.1 Structural transformation induced by SW-type trans- formation . . . . .	19
3.3.2 Structural transformation induced by Carbon-dimer evaporation . . . . .	21

3.3.3	Observation of corresponding structure transformation in TEM experiments . . . . .	25
3.4	Summary . . . . .	27
<b>IV.</b>	<b>Aluminum hydroxide as a two dimensional layered material</b>	<b>31</b>
4.1	Introduction . . . . .	31
4.2	Calculation Methods . . . . .	32
4.3	Results and Discussion . . . . .	33
4.3.1	Crystal structure of aluminum Hydroxide . . . . .	33
4.3.2	Electronic band structure of Gibbsite, Bayerite & Single Layer . . . . .	36
4.3.3	Alkali-halide Intercalated Al(OH) <sub>3</sub> . . . . .	39
4.3.4	Electronic band structure of alkali-halide intercalated Al(OH) <sub>3</sub> . . . . .	41
4.4	Summary . . . . .	42
<b>V.</b>	<b>Summary</b> . . . . .	<b>51</b>
	<b>Bibliography</b> . . . . .	<b>53</b>
	<b>Abstract in Korean</b> . . . . .	<b>63</b>

# List of Figures

Figure 3.1. A periodic supercell containing 218 carbon atoms used to model polycrystalline graphene with grain boundary. In a supercell there are two grain boundary due to fulfill the periodic boundary condition. . . . . 17

Figure 3.2. The motion of a GB by a SW-type rotation of a carbon dimer (green colored). (a) Before and (b) after the transformation. . . . . 18

Figure 3.3. The structural change process during the evaporation of a carbon dimer. (a) Corrugated graphene is formed when the distance from the graphene sheet to one of the carbon atoms in the target bond (green) is increased. (b) The top carbon atom in the target bond becomes the adatom of the other carbon atom in the target bond. (c) After the evaporation of a carbon dimer, a new grain boundary is created. (d) Energy curve for the evaporation-induced transformation. . . . . 20

Figure 3.4. Steps for stabilizing the grain boundary structure. (a) New grain boundary structure after the evaporation of a carbon dimer. (b) Grain boundary structure after one SW-type transformation. (c) Final structure after the stabilizing steps through two SW-type transformations. (d) Energy curve for the stabilizing steps. Green (blue) indicates the dimer before (after) SW-type transformation. . . . . 23

Figure 3.5. Migration of grain boundary by SW-type transformation is found in (a)–(b). The kinetic energy barrier is 7.23 eV and the total energy of configuration (a) is lower than that of configuration (b) by 2.34 eV. Migration of grain boundary by evaporation of a carbon dimer and stabilizing steps is found in (c)–(d). The energy barrier of evaporation is about 11.38 eV and the total energy of configuration (c) is lower than that of configuration (d) by 8.39 eV. . . . . 24

Figure 3.6. The HRTEM images of grain boundary between two grains of graphene. The images are taken during 11 min exposed by electron beam of which rate from a to h is  $1.0 \times 10^6 e/(nm^2s)$  and this electron beam is operated at 80kV As we can check from panel (a), grain boundaries seem enlarged pentagon and hexagon. But the length scale is same as original ones. Printed with the kind permission of authors of Ref. 1.(should be corrected(ref form)) . . . . . 25

Figure 3.7. The images for migration of grain boundary due to SW type transformation. The carbon bonds which are represented by red color are rotated  $90^\circ$  degree and it shows similar transformation to Fig.1. and Fig.4.(a) and (b) in main text. Printed with the kind permission of authors of Ref. 1. . . . . 26

Figure 3.8. The images for migration of grain boundary due to evaporation of carbon dimer and twice SW type transformations. The carbon dimer which is indicated by red color is evaporated and the green colors indicate the  $90^\circ$  degree rotation of carbon dimer. Those show similar transformation to Fig.2 and Fig.3. and similar migration of grain boundary with Fig.4.(c) and (d) in main text. Printed with the kind permission of authors of Ref. 1. . . . . 29

Figure 4.1. Crystal structure of (a) Bayerite and (b) Gibbsite. two phases have the same building block for layered structure. the same single layer is indicated in red rectangle in each Bayerite and Gibbsite crystal structure. (c),(d) Opposite sides of single layer  $A(OH)_3$  (A, B side). Drawing octahedron show different direction of oxygen around aluminum at each side. (d),(e) Stacking sequence of Bayerite and Gibbsite. Bayerite is stacked by AB-AB and Gibbsite is stacked by AB-BA squaence. . . . . 44

Figure 4.2. Electronic band structure and their projected density of states.(PDOS) of (a) Bayerite and (b) Gibbsite. Bayerite is a direct gap insulator with 5.54eV and Gibbsite is a indirect gap insulator with 5.27eV. In both materials, valence bands are mostly composed of oxygen p-orbital. Conduction bands contain oxygen s,p, aluminum s, hydrogen s, p-orbitals. . . . . 45

Figure 4.3. (a) Crystal structure of single layer  $\text{Al}(\text{OH})_3$ . (b) Top view of single layer  $\text{Al}(\text{OH})_3$ . (c) electronic band structure of single layer  $\text{Al}(\text{OH})_3$ (red) with bulk spectrum(grey) projected to two-dimensional Brillouin zone of single layer. (d) electronic band structure of bayerite-type 2, 4, 6-layered slab geometry with 2D-projected bulk spectrum (e) electronic band structure of gibbsite-type 2, 4, 6-layered slab geometry with 2D-projected bulk spectrum. . . . . 46

Figure 4.4. (a) Charge density of conduction band edge of single-layered  $\text{Al}(\text{OH})_3$ . (b) Charge density of conduction band edge of multi-layered  $\text{Al}(\text{OH})_3$ . In both cases, electrons are localized near surface atoms in outermost layers or even outside of the layer. (c) Localization of surface state in slab structure calculation based on PDOS analysis. surface region is defined as most upper and lower layer. . . . . 47

Figure 4.5. Crystal structure of Alkali-halide intercalated  $\text{Al}(\text{OH})_3$ . Alkali metal is located at the center of Al hexagon and halogen atom is at the center of Alkali metals. Lattice constants are determined by atomic radius of intercalated atoms. . . . . 48

Figure 4.6. (a) Electronic band structure and PDOS for Li-halide intercalated  $\text{Al}(\text{OH})_3$  (Cl, Br, I case from the left to right panel). (b) relative ratio of oxygen p and halide p orbital (Cl, Br, I case from the left to right panel) in valence bands. the size of dot is proportional to the occupation of atomic orbital in bloch state. . . . . 49

# List of Tables

Table 1. Unitcell information for layered structure and single layer of Al(OH) <sub>3</sub> . . . . .	36
Table 2. Unitcell information and binding energy of alkali-halide intercalated Al(OH) <sub>3</sub> . . . . .	41



# Chapter 1

## Introduction

Since the single layer graphite, called as graphene, is discovered [1], there was large interest to 2D materials or layered materials. There have been many researches on single layer and few layer graphene [1–5], hexagonal Boron Nitride(h-BN) [6–10] and various Transition metal dichalcogenides(TMDs) [11–13]. Especially, graphene has a unique band structure containing Dirac cone, which shows linear dispersion at K-point resulting in high electron mobility. So graphene was considered as the most promising material for future nano electronic devices. So, numerous studies have investigated focused on graphene including its electrical, mechanical and optical properties and for industrial usage, the synthesis of large area graphene is also intensely researched. The most productive way was Chemical vapor deposition (CVD) method [5]. However, in this method, graphene usually grows with multiple grain with random orientation accompanied by the formation of various types of grain boundaries(GBs) [5, 14, 15]. The properties of graphene can significantly change depending on the types of GBs [16–19]. Forming GBs in a controllable manner may provide a route for tailoring the properties of CVD graphene. Previous studies have shown that the GBs in graphene can created affected by temperature [20], pressure, substrate [21], grain seeds [22], and electron beam irradiation [23,24]. However, the atomistic mechanisms responsible for the GB motion in graphene

have not yet been sufficiently explored. In this paper, we present atomistic models for the motions of GBs observed during TEM experiments. Based on first-principles calculations, we show that GBs can migrate through a series of Stone-Wales (SW)-type transformations, which can occur much more easily near the GBs than in pristine graphene. We also show that GBs can drive the evaporation of a carbon dimer, which has a greatly reduced energy barrier due to the lattice mismatch (or intrinsic strain fields) at the GBs. Our findings contribute to the understanding of GB motion under electron beam irradiation, and thus, they may guide experimental efforts for controlling GBs in CVD graphene and for tailoring the material properties of CVD graphene. It would be the first subject handled in this thesis.

In addition to 2D material, there are also lots of interest in few-layer case and layered material [1–13]. In case of layered material, stacking sequence and number of stacked layer have large effect to their physical properties. for example, there was direct to indirect gap change in  $\text{MoS}_2$  [25] depending on number of layer. Number of layer and stacking dependent band structure in few-layer graphene and staking dependent band structure and optical properties in heterostructure were also reported. In addition to fundamental researches, 2d single-layered or multi-layered materials have been studied due to their potential in application, for example, in energy storage [26, 27], gas absorption, catalyst [28] and energy conversion [27] represented by solar cell. The layered structure material abovementioned have a common point that they are having van der Waals(vdW) interaction as interlayer binging mechanism. However, there is other candidate for weak interlayer binding mechanism. So, we found the layered structure of  $\text{Al}(\text{OH})_3$

with hydrogen bonding as interlayer binding and studied on their crystal structure and electronic structure showing stacking and number of stacked layer dependent properties. Layered structure  $\text{Al}(\text{OH})_3$  have been mentioned several times with experiments and calculation(ref), however, their properties as a layered material and their electronic band structure has not been noticed enough. The study on  $\text{Al}(\text{OH})_3$  would be the second subject in this thesis.



# Chapter 2

## Computational Methods

### 2.1 Density Functional Theory

Electronic band structures determine diverse physical properties in condensed matter. It could provide not only an intuition for understanding materials and physics underneath, but also give the way of quantitative research. Condensed matter system contains many electrons so should solve many-body Schrödinger equation to obtain its electronic band structure with Many-body Hamiltonian  $H$ .

$$H\Psi = E\Psi$$
$$H = -\sum_i \frac{\hbar^2}{2m_e} \nabla_i^2 - \sum_I \frac{\hbar^2}{2m_I} \nabla_I^2 + \frac{1}{2} \sum_{I \neq J} \frac{Z_I Z_J e^2}{|\mathbf{R}_I - \mathbf{R}_J|} + \frac{1}{2} \sum_{i,l} \frac{Z_l e^2}{|\mathbf{r}_i - \mathbf{R}_l|} + \frac{1}{2} \sum_{i \neq j} \frac{e^2}{|\mathbf{r}_i - \mathbf{r}_j|}$$

In a Many-body Hamiltonian, the first and second terms are kinetic contributions of electrons and nuclei. Other terms are Coulomb interaction terms contributed from nucleus-nucleus, nucleus-electron, electron-electron interactions. To fully describe these interacting terms is difficult and computationally expensive. There have been many methods to obtain electronic band

structure. In many ways, Density functional theory(DFT) has been great success due to splendid Hohenberg-Kohn theorem [29] and Kohn-Sham equation combined with various functionals and type of pseudopotentials. The essential theorem and equation of DFT is written in following sections.

### 2.1.1 Hohenberg-Kohn Theorem

**Theorem 1.** The ground state particle density  $n_0(\mathbf{r})$  uniquely determines potential  $V_{ext}(\mathbf{r})$ , except for a constant, for any system of interacting particles in an external potential  $V_{ext}(\mathbf{r})$

**Proof** Suppose that there are two different external potentials  $V_1(\mathbf{r})$  and  $V_2(\mathbf{r})$ , which differ by more than a constant and gives the same ground state density  $n_0(\mathbf{r})$ . Two different hamiltonian comes from these two external potential, which gives different ground state wavefunctions  $\Psi_1(\mathbf{r})$  and  $\Psi_2(\mathbf{r})$ . Then, it gives following inequality because  $\Psi_2(\mathbf{r})$  is not a ground state of  $H_1$

$$E_1 = \langle \Psi_1 | H_1 | \Psi_1 \rangle < \langle \Psi_2 | H_1 | \Psi_2 \rangle \quad (2.1)$$

The last term in eq.(7) can be written as

$$\begin{aligned} \langle \Psi_2 | H_1 | \Psi_2 \rangle &= \langle \Psi_2 | H_2 | \Psi_2 \rangle + \langle \Psi_2 | H_2 - H_1 | \Psi_2 \rangle \\ &= E_2 + \int d\mathbf{r} [V_1(\mathbf{r}) - V_2(\mathbf{r})] n_0(\mathbf{r}) \end{aligned}$$

as a result,

$$E_1 < E_2 + \int d\vec{r}[V_1(\mathbf{r}) - V_2(\mathbf{r})]n_0(\mathbf{r}) \quad (2.2)$$

We also get another inequality by the same procedure with exchanged subscript 1 and 2,

$$E_2 < E_1 + \int d\vec{r}[V_2(\mathbf{r}) - V_1(\mathbf{r})]n_0(\mathbf{r}) \quad (2.3)$$

After adding two results, we finally get the inequality  $E_1 + E_2 < E_1 + E_2$ , which is contradict. So, The ground state particle density  $n_0(\mathbf{r})$  uniquely determines potential  $V_{ext}(\mathbf{r})$ , except for a constant, in turn, Hamiltonian is also uniquely determined within a constant

**Theorem 2.** Since all properties such as kinetic energy and interaction energy terms are uniquely determined if  $n(\mathbf{r})$  is specified, we can easily define total energy functional  $E[n]$  and the density  $n(\mathbf{r})$  minimizing this functional is exactly same as ground state density  $n_0(\mathbf{r})$

**proof**

$$\begin{aligned} E_{HK}[n] &= T[n] + E_{int}[n] + \int d^3\vec{r}V_{ext}(\mathbf{r})n(\mathbf{r}) + E_{II} \\ &\equiv F_{HK}[n] + \int d^3\vec{r}V_{ext}(\mathbf{r})n(\mathbf{r}) + E_{II} \end{aligned}$$

where,  $E_{II}$  is the interaction energy of the nuclei and  $F_{HK}[n]$  is an universal functional including all internal energies, kinetic and potential of the interacting electron system. Now, consider a system with the ground state

density  $n_1(\mathbf{r})$ , which gives corresponding external potential  $V_1(\mathbf{r})$ , Hamiltonian  $H_1$ , ground wavefunction  $\Psi_1$ . with all the result from ground state density, we could get the Hohenberg-Kohn functional value with ground state density same as expectation value of unique ground state Hamiltonian  $H_1$

$$E_1 = E_{HK}[n_1] = \langle \Psi_1 | H_1 | \Psi_1 \rangle \quad (2.4)$$

Now, consider another different density,  $n_2(\mathbf{r})$ , which necessarily makes a different wavefunction  $\Psi_2$ . the expectation value with  $\Psi_2$  and ground state Hamiltonian  $E_2$  should be greater than the energy from Hohenberg-Kohn functional evaluated with correct ground state density  $n_0(\mathbf{r})$ . It says that if the Hohenberg-functional was known, then the density minimizing the total energy functional is exactly ground state density and the energy functional value is ground state energy.

### 2.1.2 Kohn-Sham equation

The Hohenberg-Kohn Theorem changes essential variable from the wavefunction to electron density, to find ground state density is another problems for solving many-electron Hamiltonian. By considering Kohn-Sham ansatz, we could map the difficult many body interacting system onto non-interacting auxiliary system. Kohn-Sham ansatz has two assumptions.

1. The exact ground state density can be represented by the ground state density of an auxiliary system of non-interacting particles.
2. The auxiliary hamiltonian is chosen to have the usual kinetic operator and

an effective local potential  $V_{eff}(\mathbf{r})$

By mapping the interacting system onto auxiliary independent-particle system, we can write the density of the auxiliary system as sums of squares of the orbitals  $n(\mathbf{r}) = \sum_i |\psi_i(\mathbf{r})|^2$ . Then, the Hohenberg-Kohn expression for the ground state can be rewritten as the following form.

$$E_{KS} = T_s + \int d\mathbf{r} V_{ext}(\mathbf{r})n(\mathbf{r}) + E_{Hartree}[n] + E_{II} + E_{xc}[n] \quad (2.5)$$

where  $T_s$  is the independent-particle kinetic energy

$$T_s = -\frac{1}{2} \sum_{i=1}^N \langle \psi_i | \nabla^2 | \psi_i \rangle = -\frac{1}{2} \sum_{i=1}^N |\nabla \psi_i(\mathbf{r})|^2 \quad (2.6)$$

the exchange-correlation energy  $E_{xc}$  contains remaining term of kinetic energy of interacting system and many-body interacting effects. If the universal functional  $E_{xc}[n]$  was known, then the exact ground state energy and density of the many-body electron problem could be obtained by solving the Kohn-Sham equation for non-interacting system. From the Hohenberg-Kohn theorem 2, we could obtain ground state density and energy by minimizing the Kohn-Sham energy expression [30].  $\frac{\delta E_{KS}}{\delta \psi_i^*(\mathbf{r})} = 0$  with the orthonormal constraints  $\langle \psi_i | \psi_j \rangle = \delta_{i,j}$  by Lagrange multiplier method. All this procedure leads the Kohn-Sham Schrodinger-like equation.

$$(H_{KS}(\mathbf{r}) - \epsilon_i)\psi_i(\mathbf{r}) = 0 \quad (2.7)$$

where the  $H_{KS}$  is the effective hamiltonian

$$H_{KS}(\mathbf{r}) = -\frac{1}{2}\nabla^2 + v_{eff}(\mathbf{r}) \quad (2.8)$$

and

$$\begin{aligned} v_{eff}(\mathbf{r}) &= v_{ext}(\mathbf{r}) + \frac{\delta E_{Hartree}}{\delta n(\mathbf{r})} + \frac{\delta E_{xc}}{\delta n(\mathbf{r})} \\ &= v_{ext}(\mathbf{r}) + v_{Hartree}(\mathbf{r}) + v_{xc}(\mathbf{r}) \end{aligned}$$

### 2.1.3 The Approximation of Exchange-correlation Functional : LDA and GGA Approximation

As mentioned above section, Hohenberg-Kohn theorem and Kohn-Sham ansatz gives exact mathematical formalism, However, without specific form of exchange-correlation functional  $E_{xc}[n]$ , it could not be used in a practical way. So, there are many trying to approximate the unknown exchange-correlation functional. Local density approximation(LDA) started from the exchange-correlation in locally homogeneous electron gas. In this approximation, inhomogeneous gas considered as homogeneous gas having locally constant density. Exchange-correlation energy  $E_{xc}$  can be expressed in the intergrated form with exchange-correlation energy density  $\epsilon_{xc}$

$$E_{xc}[n] = \int d\mathbf{r} n(\mathbf{r}) \epsilon_{xc}([n], \mathbf{r}) \quad (2.9)$$

exchange-correlation energy density  $\epsilon_{xc}$  could be seperated to two contribution, the exchange energy  $\epsilon_x$  and the correlation energy  $\epsilon_c$ . the

exchange energy of the homogeneous gas is well known from simply analytic calculation.

$$\epsilon_x[n] = -\frac{3}{4\pi}k_F = -\frac{3}{4\pi}\left(\frac{6}{\pi}n(\mathbf{r})\right)^{\frac{1}{3}} \quad (2.10)$$

and the correlation energy has been obtained from quantum Monte Carlo methods [31]. In LDA approximation, there are a lot of version for fitting to numerical correlation energy for homogeneous gas. For example, Hedin-Lundqvist(HL) [32], Perdew-Zunger(PZ) [33], Vosko-Wilkes-Nusiar(VWN) [34], etc. Success of LDA exchange-correlation functional has proven the value of Density functional Theory and also stimulated the improved functionals. Generalized-gradient approximations(GGA) is the first step to improve beyond LDA, in this functional the gradient of density  $|\nabla n|$  is also considered additional to density  $n$ .

$$E_{xc}^{GGA}[n^\sigma] = \sum_{\sigma} \int d^3\mathbf{r} n(\mathbf{r}) \epsilon_{xc}(n^\sigma, |\nabla n^\sigma|, \dots) \quad (2.11)$$

In GGA approximation, exchange energy  $E_x^{GGA}$  is handled by the homogeneous exchange energy density  $\epsilon_x^{LDA}$  with enhancement factor  $F_x(s)$ , where  $s = \frac{|\nabla n^\sigma|}{(2k_f)n}$ . Correlation energy could be corrected by high order density gradient term. There are various form of considering gradient of the density  $|\nabla n^\sigma|$ . The specific form of exchange and correlation energy density made by Perdew and Burke and Ernzerhof(PBE) [35] is given as follow.

$$E_x^{PBE}[n] = \int d\mathbf{r} \epsilon_x^{hom}(n(\mathbf{r})) F_x(s) \quad (2.12)$$

where,

$$F_x(s) = 1 + \kappa - \frac{\kappa}{1 + \mu s^2 / \kappa}, \kappa = 0.804, \mu = 0.21951 \quad (2.13)$$

Correlation energy in GGA-PBE is described by

$$E_c^{PBE}[n^\uparrow, n^\downarrow] = \int d\mathbf{r} [\epsilon_x^{hom}(r_s, \zeta) + H(r_s, \zeta, t)]$$

$$H = \frac{e^2}{a_0} \gamma \phi^3 \log\left(1 + \frac{\beta}{\gamma} t^2 \frac{1 + At^2}{1 + At + A^2 t^4}\right)$$

where,  $A = \frac{\beta}{a_0} [\exp(\frac{-\xi_c^{hom}}{\gamma \phi^3 \frac{e^2}{a_0}}) - 1]^{-1}$ , with  $a_0$  is a Bohr radius,  $\zeta = (n^\uparrow - n^\downarrow)/n$  is the spin polarization,  $r_s$  is the local value of the density paramter, and  $t$  is a dimensionless gradient  $t = |\nabla n| / 2\phi k_F n$  with  $\phi = ((1 + \zeta)^{\frac{2}{3}} + (1 - \zeta)^{\frac{2}{3}}) / 2$

## 2.2 The plane wave basis sets and Pseudopotential

### 2.2.1 Plane wave basis

To solve the many body Schrodinger equation or one particle Kohn-Sham equation of given solid system numerically, it is general to introduce a appropriate basis set to expand the unknown wavefunction. In a solid with periodic potential, Bloch theorem gives the wavefunction introducing wave

vector  $\mathbf{k}$ , which is Fourier transformed as follow.

$$\Psi_{\mathbf{k}}(\mathbf{r}) = \frac{e^{i\mathbf{k}\cdot\mathbf{r}}}{\sqrt{\Omega}} \sum_{\mathbf{G}} c_{\mathbf{k}}(\mathbf{G}) e^{i\mathbf{G}\cdot\mathbf{r}} \quad (2.14)$$

where,  $\mathbf{G}$  is Reciprocal lattice vector satisfying the relation  $e^{i\mathbf{G}\cdot\mathbf{a}_i}$  with lattice vector  $\mathbf{a}_i$ . i.e.  $\mathbf{G}\cdot\mathbf{a}_i = 2n\pi$  for  $i = 1, 2, 3$  in three dimensional space. From the abovementioned expansion of wavefunction, we can define the plane wave basis set as

$$\phi_{\mathbf{G}}(\mathbf{r}) = \frac{e^{i\mathbf{G}\cdot\mathbf{r}}}{\sqrt{\Omega}} \quad (2.15)$$

This basis set also satisfy the normalization condition for intergration over given unitcell.

## 2.2.2 Projector augmented waves(PAW) method

The electrons in condensed matter can be classified by two kinds. first one is core electron and another one is valence electron. core electrons are strongly binded and have higher kinetic energy than valence electrons showing oscillatory behavior of wavefunction. So, it spend computational cost much to describe the core electron with plane wave basis set. Therefore, for the system where core variation of core electron is negligible, we can reduce the computational cost remarkably by replacing the potential from core electron. It is the main idea for psuedopotential approximation. The pseudopotential replaces the core potential showing the coincidencde of scattering properties with all-electron potential. the scattering properties are satisfied

by the matching of phase shift up to  $2\pi$  due to pseudized potential supposing localized spherical potential at any energy with that due to all electron potential. Then all the scattering properties including cross-section and behavior of wavefunction outside the scattering region coincide. There is one way to pseudize the core potential known as Projector augmented waves (PAWs), which characteristics is keeping the full wavefunction using appropriate projector form. In PAW approach, it introduces projectors and auxiliary localized functions like the "ultrasoft" pseudopotential method and reformulates the Orthogonalized plane waves (OPWs) possible for calculation of total energy, forces, and stress with modern techniques. For describing valence electron, there can be a relation between smooth part of a valence wavefunction  $\tilde{\psi}$  and all-electron valence function  $\psi$  like as  $\psi = T\tilde{\psi}$  with linear transformation  $T$ .

$$T = 1 + \sum_m \{ |\psi_m\rangle - |\tilde{\psi}_m\rangle \} \langle \tilde{p}_m | \quad (2.16)$$

where, a set of projection operator  $\tilde{p}$  gives the coefficient of partial waves  $m$  for each sphere as  $c_m = \langle \tilde{p}_m | \tilde{\psi} \rangle$  and satisfying the biorthogonality condition  $\langle \tilde{p}_m | \tilde{\psi}_{m'} \rangle = \delta_{mm'}$ . Due to this linear transformation including the full all-electron wavefunction, any operator  $\hat{A}$  can be transformed to operator acting on smooth part of the wavefunctions, which finally gives the expectation values of operator for smooth part of the wavefunctions.

$$\tilde{A} = \hat{A} + \sum_{mm'} |\tilde{p}\rangle \{ \langle \psi_m | \hat{A} | \psi_{m'} \rangle - \langle \tilde{\psi}_m | \hat{A} | \tilde{\psi}_{m'} \rangle \} \langle \tilde{p}_{m'} \quad (2.17)$$

## Chapter 3

# Atomic-scale investigation of grain boundary motion in graphene

### 3.1 Introduction

Since the first isolation of a single atomic layer of graphite, which is known as graphene [1], numerous studies have investigated its outstanding material properties from many perspectives, including its electrical [1–5], mechanical [36, 37], and optical properties [38–44]. In particular, the synthesis of large-area graphene using the chemical vapor deposition (CVD) method [5] was a great achievement that has accelerated the realization of applications for graphene [45]. The CVD methods have also provided new possibilities for controlling the properties of graphene due to its polycrystalline nature. It has been found that graphene grown using CVD methods (CVD graphene) is highly likely to form multiple grains accompanied by the formation of various types of grain boundaries (GBs) [5, 14, 15]. The properties of graphene can significantly change depending on the types of GBs present in the CVD graphene sample [16–19]. Forming GBs in a controllable manner may provide a route for tailoring the properties of CVD graphene. Previous studies have shown that the GBs in graphene can migrate as a result of temperature [20], pressure, substrate [21], grain seeds [22], and electron

beam irradiation [23, 24]. However, the atomistic mechanisms responsible for the GB motion in graphene have not yet been sufficiently explored. In this paper, we present atomistic models for the motions of GBs observed during TEM experiments. Based on first-principles calculations, we show that GBs can migrate through a series of Stone-Wales (SW)-type transformations, which can occur much more easily near the GBs than in pristine graphene. We also show that GBs can drive the evaporation of a carbon dimer, which has a greatly reduced energy barrier due to the lattice mismatch (or intrinsic strain fields) at the GBs. Our findings contribute to the understanding of GB motion under electron beam irradiation, and thus, they may guide experimental efforts for controlling GBs in CVD graphene and for tailoring the material properties of CVD graphene.

## 3.2 Computational Details

We performed ab initio total energy calculations using the generalized gradient approximation of the Perdew-Burke-Ernzerhof (GGA, PBE) exchange-correlation functional [46] and projected augmented wave pseudopotentials [47] as implemented in the VASP code [48]. The kinetic energy cutoff was set to 450 eV. A periodic supercell containing 218 carbon atoms was used to model polycrystalline graphene. In our calculation, to fulfill the periodic boundary conditions, we placed two equally distanced GBs in a supercell. In the total energy calculation for the change of GB structures, the structural changes are applied to only one of the two GBs while the second GB introduced for periodicity remains intact. The unitcell used for

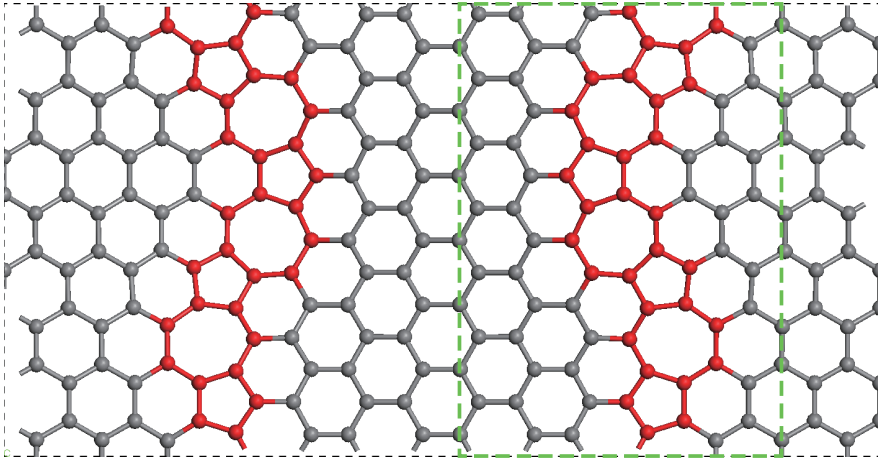


Figure 3.1: A periodic supercell containing 218 carbon atoms used to model polycrystalline graphene with grain boundary. In a supercell there are two grain boundary due to fulfill the periodic boundary condition.

calculation is shown in Fig. 3.1 The GB was modeled as a periodic array of pentagon and heptagon pairs, as shown in Fig. 3.1(a). This type of grain boundary was previously suggested in the literature [17] and is known to have the lowest formation energy for a given lattice misorientation angle of  $\approx 30^\circ$ . To determine the energy barrier for the SW-type transformation, the orientation of the dimer relative to the coordinate axis was divided into small in-plane angles from the initial to the final configuration and was fixed for each total energy calculation. To determine the energy barrier for the dimer evaporation, we calculate the total energy by gradually pulling up the carbon dimer under the constraint of fixed distance between the objective dimer and

the binding atom. In this calculation, the other atoms were fully relaxed.

### 3.3 Result and discussion

We found two main mechanism for structural transformation in graphene grain boundary. One is SW-type transformation and the other is Carbon-dimer evaporation. Former conserves the number of atoms in graphene with grain boundary, however, latter one make changes in number of atoms. Combination of these two kinds of transformation can induce diverse structural transformations by inserted energy from accelerated electron beam. We analyze these transformations and find the energy barrier of each structure transformation.

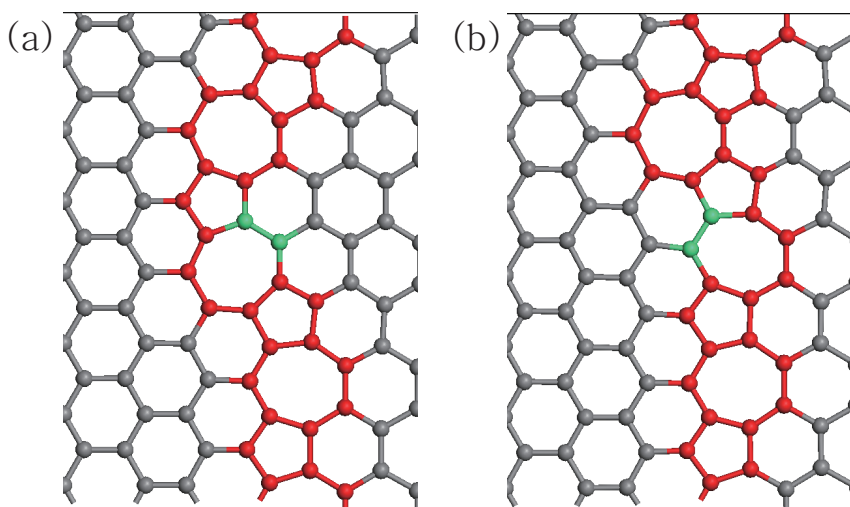


Figure 3.2: The motion of a GB by a SW-type rotation of a carbon dimer (green colored). (a) Before and (b) after the transformation.

### 3.3.1 Structural transformation induced by SW-type transformation

The SW-type transformation, an in-plane  $90^\circ$  rotation of a carbon dimer, has already been reported in pristine graphene and in the reconstruction process of divacancy defects [49–51]. Figure 1 shows the motion of a GB induced by such a SW-type transformation. A GB forms between two tilted grains with a misorientation angle of  $\sim 30^\circ$  as a one-dimensional chain of pentagon and heptagon defects. The motion of a GB can be understood as the motions of the 5-7 defects that form the GB, which can be induced by a single SW-type rotation of carbon dimers. For example, a single SW-type rotation of a carbon dimer, which is colored in green in Fig. 3.2, changes the position of the 5-7 defect from the left-hand side of the dimer to the right-hand side, resulting in the grain boundary moving to the right-hand direction. We hypothesized that this event can occur under electron beam irradiation during TEM measurements. We found that the energy barrier for the rotation of the dimer is 7.23 eV. Note that the maximum kinetic energy transfer from incident electrons to a carbon atom is  $\sim 15.8$  eV when using a 80 keV TEM [52]. The SW-type transformation occurs much easier near the GBs than in pristine graphene because its energy barrier is lower by 2 eV than that of pristine graphene, which has been reported as 9.2 eV [53, 54]. The lowered energy barrier for the SW-type transformation is plausible when considering the intrinsic strain concentrated on the 5-7 defects that form the GB. The intrinsic strain due to the lattice mismatch between tilted grains should reduce the bonding strength at the GB, thereby facilitating the rota-

tion of the dimer. Note that the structure after the rotation [Fig. 3.2 (b)] has a 2.34 eV larger total energy than the structure before the rotation [Fig. 3.2 (a)]

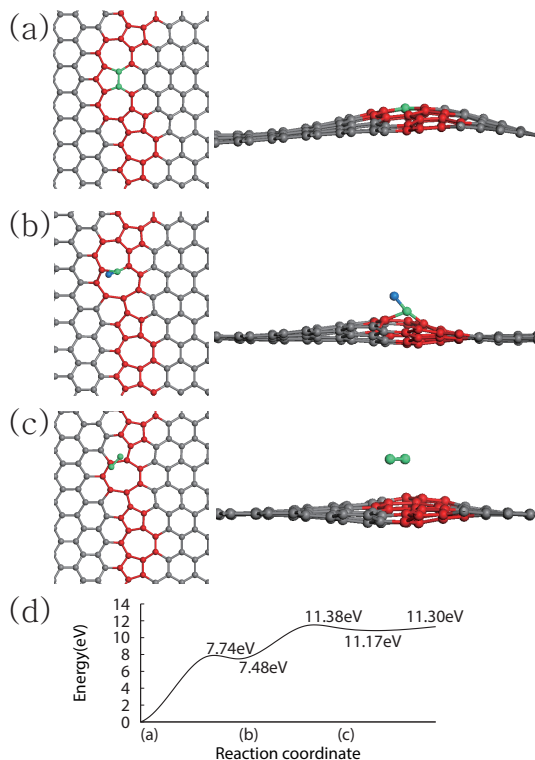


Figure 3.3: The structural change process during the evaporation of a carbon dimer. (a) Corrugated graphene is formed when the distance from the graphene sheet to one of the carbon atoms in the target bond (green) is increased. (b) The top carbon atom in the target bond becomes the adatom of the other carbon atom in the target bond. (c) After the evaporation of a carbon dimer, a new grain boundary is created. (d) Energy curve for the evaporation-induced transformation.

### 3.3.2 Structural transformation induced by Carbon-dimer evaporation

GBs in polycrystalline graphene can also migrate as a result of the evaporation of carbon atoms, as previously reported from tight-binding molecular dynamics simulations of graphene and graphene nanoribbons [55, 56]. We propose an atomistic process for the evaporation of a carbon dimer at the GB, which consists of a few atomistic steps characterized by the corresponding configuration energy curves presented in Fig. 3.3 (d). During the first step [from Fig. 3.3 (a) to the first maximum in Fig. 3.3 (d)], a carbon dimer that forms a 5-7 defect [green colored in Fig. 3.3 (a)] in the region where an intrinsic strain is concentrated increases in height above the graphene sheet and forms a bump, as shown in Fig. 3.3 (a). The formation of bump in GB has been reported by ab initio calculation. Note that the formation of this bump is possible due to the presence of intrinsic strain originating from the lattice mismatch between the tilted grains. The total energy gradually increases during this process, as indicated by the slope starting from (a) in Fig. 3.3 (d). As the top of the bump reaches  $\approx 2 \text{ \AA}$  from the graphene sheet (the first maximum), one of the two carbon atoms that form the dimer [blue colored in Fig. 3.3 (b)] breaks free of the bond and becomes an adatom that is attached to the other carbon atom of the dimer, as shown in Fig. 3.3 (b). In this configuration, the total energy forms a local minimum (b), as shown in Fig. 3.3 (d). As the height of the adatom increases, the total energy also increases. As the height of the bump reaches  $2.99 \text{ \AA}$  (the 2nd maximum), the bond between the other carbon atom and the graphene breaks and the

dimer becomes isolated from the sheet as shown in Fig. 3.3 (c). The energy barriers from (a) to (b) and from (b) to (c) are 7.74 and 3.90 eV, respectively. The evaporation of the carbon dimer can occur more easily through the formation of the adatom. The overall energy barrier for the evaporation of the dimer (11.38 eV) is considerably reduced compared to the evaporation of an atom in sp<sup>2</sup>-bonded carbon (18-20 eV) [57, 58]. The energy barrier is also smaller than the maximum energy (15 eV) transferred at 80 kV radiation in the TEM and the evaporation of carbon dimer would be possible at the grain boundary. Even though our simulations are performed for GB with a misorientation angle of 30°, the evaporation of carbon dimer can be observed in other types of GB which are composed of 5-7 pairs because the energy barrier (10.3 eV) [59] for the dimer evaporation at 5-7 pair is similar as our result. The GB structure after the evaporation of a carbon dimer can be further stabilized through a series of SW-type transformations, resulting in motion of the GB. As shown in Fig. 3.3 (c), after the evaporation of the dimer, the system is no longer a one-dimensional chain of 5-7 defects, which indicates that the system can be further stabilized into a one-dimensional chain of 5-7 defects, thereby fully relaxing the intrinsic strain. Guided by this observation, we can consider the possible transformations that stabilize the structure. We find that this type of chain geometry can be realized by two consecutive SW-type transformations, as shown in Fig. 3.4. In Fig. 3.4, the blue color indicates the carbon dimer that has been rotated after a SW-type transformation, and the green color indicates the carbon dimer that will be rotated. After the first SW-type transformation, one heptagon and three hexagons are changed into two heptagons, one hexagon,

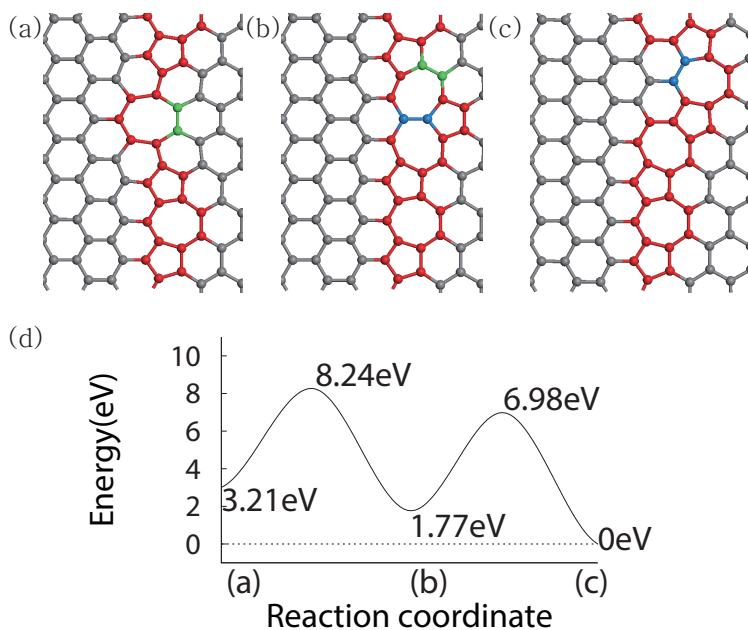


Figure 3.4: Steps for stabilizing the grain boundary structure. (a) New grain boundary structure after the evaporation of a carbon dimer. (b) Grain boundary structure after one SW-type transformation. (c) Final structure after the stabilizing steps through two SW-type transformations. (d) Energy curve for the stabilizing steps. Green (blue) indicates the dimer before (after) SW-type transformation.

and one pentagon. This 5-7 defect change the position by another SW-type transformation of a carbon dimer, as indicated in green in Fig. 3.4(b). The formation energy curve for the two consecutive SW-type transformations is presented in Fig. 3.4 (d). The energy barriers for the first and second transformations are 5.03 and 5.21 eV, respectively. As shown in Fig. 3.4 (c), the one-dimensional chain structure of the GB is clearly restored by the two SW-type transformations, which reduces the total energy of the system. Furthermore, after the evaporation of the dimer and the two SW-type transformations, the GB migrates to the right. This structural change requires a

total of 8.39 eV. Compared to the formation energy of a divacancy in pristine graphene ( 16 eV), the presence of the GB greatly facilitates the evaporation of a dimer in polycrystalline graphene by allowing the intermediate adatom state. The structural transformations explained as SW-type transformations and the evaporation of a dimer can induce the migration of GBs, as shown in Fig. 3.5.

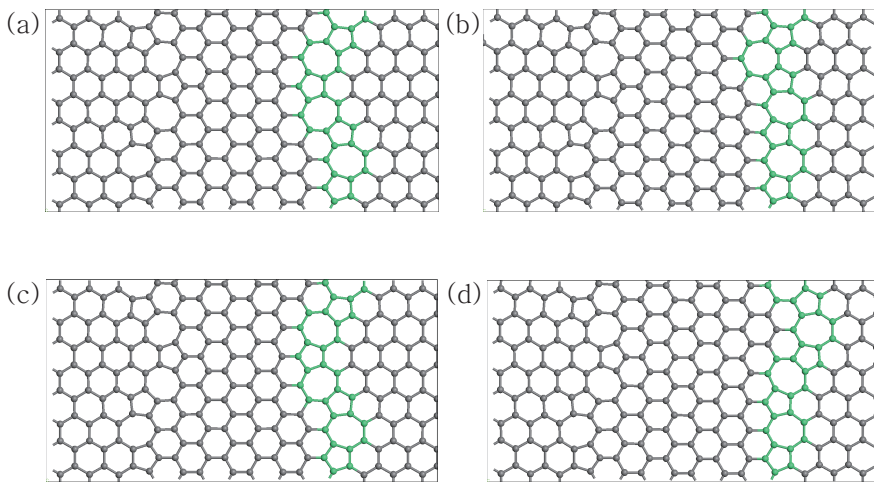


Figure 3.5: Migration of grain boundary by SW-type transformation is found in (a)–(b). The kinetic energy barrier is 7.23 eV and the total energy of configuration (a) is lower than that of configuration (b) by 2.34 eV. Migration of grain boundary by evaporation of a carbon dimer and stabilizing steps is found in (c)–(d). The energy barrier of evaporation is about 11.38 eV and the total energy of configuration (c) is lower than that of configuration (d) by 8.39 eV.

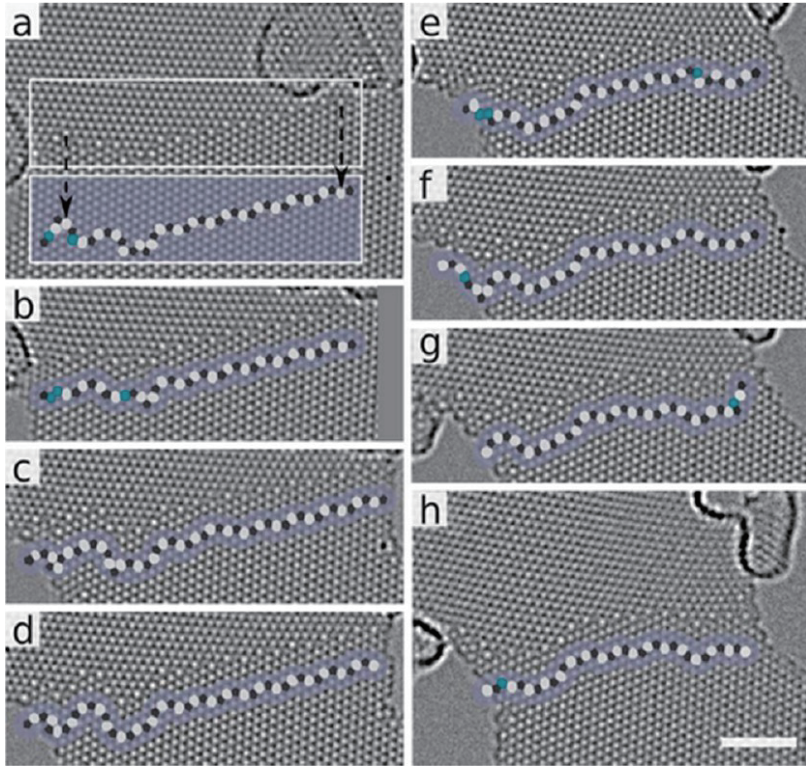


Figure 3.6: The HRTEM images of grain boundary between two grains of graphene. The images are taken during 11 min exposed by electron beam of which rate from a to h is  $1.0 \times 10^6 e/(nm^2s)$  and this electron beam is operated at 80kV As we can check from panel (a), grain boundaries seem enlarged pentagon and hexagon. But the length scale is same as original ones. Printed with the kind permission of authors of Ref. 1.(should be corrected(ref form))

### 3.3.3 Observation of corresponding structure transformation in TEM experiments

Our proposed process of dimer evaporation for grain boundary motion was found from careful analysis of the TEM images reported by Kurasch

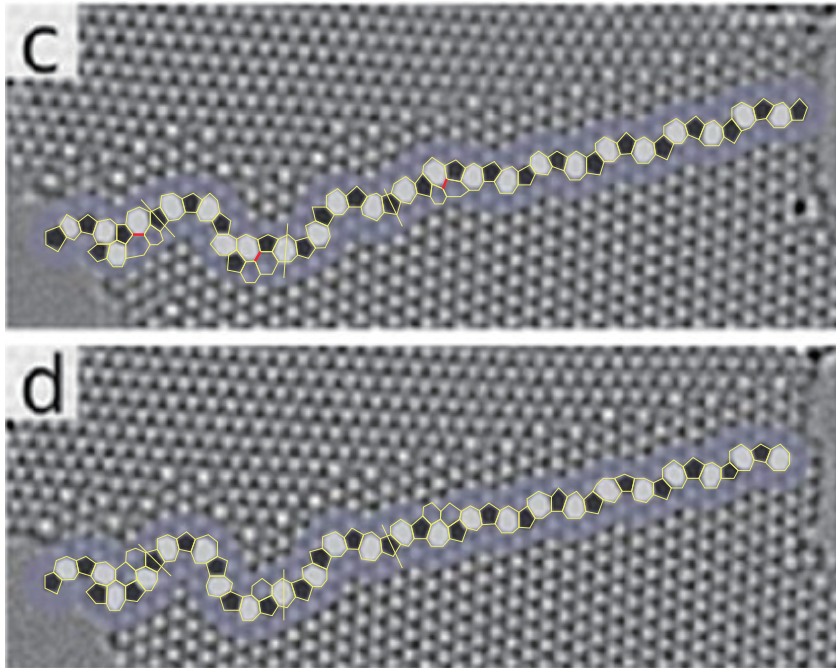


Figure 3.7: The images for migration of grain boundary due to SW type transformation. The carbon bonds which are represented by red color are rotated  $90^\circ$  degree and it shows similar transformation to Fig.1. and Fig.4.(a) and (b) in main text. Printed with the kind permission of authors of Ref. 1.

et al. Similarly to the observation of GB migration in HR-TEM, our study shows that the stable GB can fluctuate by the local motion of GB. Among these experimental data, we can find a real match with my calculation data. If we noticed the change in Fig2. (c) to Fig2(d), This migration of grain boundary can be explained well by S.W transformation. In Supplementary Figure. 3, the carbon bond which is located between heptagon and hexagon nearby pentagon is rotated by  $90^\circ$  degree as mentioned in explanation of Fig. 3.1 of the main text. Fig. 3.1 and Fig. 3.4(a) and Fig. 3.4 (b) in the main

text show an excellent agreement with Supplementary Fig. 3.3. Now check the second possible transformation, so called, evaporation of carbon dimer. It also follows the steps described in explanation of Fig. 3.2 and Fig. 3.3 in main text. Supplementary figure 4 is well describing the structural change by evaporation of carbon dimer. As mentioned in main text, the evaporation of carbon dimer and following twice SW type transformation explain very well the observation of TEM as shown in supplementary figure 4. These two types of transformation can be occurred in environments of electron beam from HRTEM which is operated at 80kV. It is very meaningful that the calculation result seems similar result in experiments which don't need very high energy.

### **3.4 Summary**

We have investigated the motion of GBs of two grains of graphene that have crystalline directions mismatched by  $30^\circ$ . This GB motion can be understood as a series of SW-type structural transformations of 5-7 defects that form the GBs. The energy barrier for the SW-type transformation is greatly reduced to 7.23 eV due to the presence of GBs. We also suggest that the GBs can easily migrate through the evaporation of a carbon dimer due to the presence of GBs. These transformations and their reduced energy barriers provide a means for microscopically controlling grain boundaries. An appropriate electron beam that has adequate energy and accuracy to specific sites provides control over grain boundary migration. The accuracy on the atomic carbon sites hit by electron beam will be more important for

the control of grain boundary migration When the motions of other types of grain boundary structures are investigated and analyzed, the ability to control grain boundaries in polycrystalline graphene will contribute to the production of graphene with better quality and larger areas.

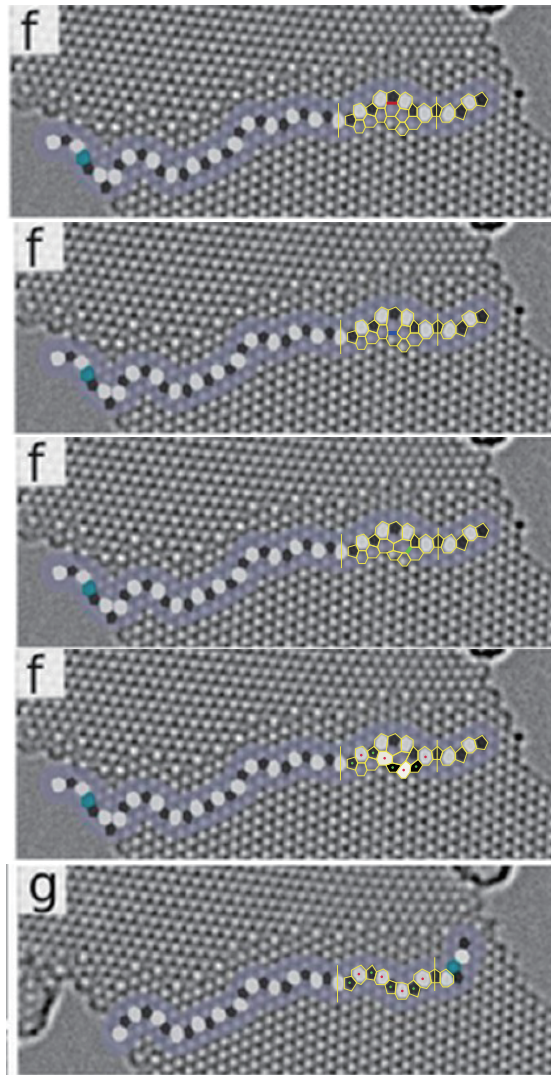


Figure 3.8: The images for migration of grain boundary due to evaporation of carbon dimer and twice SW type transformations. The carbon dimer which is indicated by red color is evaporated and the green colors indicate the  $90^\circ$  degree rotation of carbon dimer. Those show similar transformation to Fig.2 and Fig.3. and similar migration of grain boundary with Fig.4.(c) and (d) in main text. Printed with the kind permission of authors of Ref. 1.



## Chapter 4

# Aluminum hydroxide as a two dimensional layered material

### 4.1 Introduction

Since the single layer graphite, called as graphene, is discovered [1], there have been a lot of interests in 2D single-layered or multi-layered materials. Many researches on single layer or a few layer graphene [1–5], hexagonal Boron Nitride(h-BN) [6–10] and various transition metal dichalcogenides(TMDs) [11–13] were reported. In case of multi-layered material, stacking sequence and number of stacked layer have various effects to their physical properties. For example, there was transition of band gap from direct to indirect in MoS<sub>2</sub> depending on the number of layers [25]. Kinds of layer constituting heterostructures or multi-layered materials also affect the electronic band structures and optical properties. In addition to fundamental researches, 2d single-layered or multi-layered materials have been studied due to their potential in application, for example, in energy storage [26, 27], gas absorption, catalyst [28] and energy conversion [27] represented by solar cell. The abovementioned and previously reported layered structure materials have a common point that they have van der Waals (vdW) interaction as interlayer binding mechanism. However, there can be other candidates for

having other type of weak interlayer binding mechanism. We found the layered structure of  $\text{Al}(\text{OH})_3$  with hydrogen bonding as interlayer binding and studied on their crystal structure, electronic band structure and stacking and number of stacked layer dependence. Layered structure  $\text{Al}(\text{OH})_3$  have been mentioned several times with experiments and calculation [60–64], however, their properties as a layered material and their electronic band structure have not been noticed enough. In the first section of this paper, we mention about the crystal structure of two bulk phases and a single layer as a building block of layered structure and its quantitative verification as a layered material with total energy calculation using Density functional Theory (DFT). In the second section, we show their electronic band structure for single layer, few-layer and bulk structure with DFT calculation. We also introduce the characteristic surface state emergent from breaking interlayer hydrogen bonds. In the final section, we will report the result of Alkali-halide intercalation as an engineering of crystal structure and electronic band structure of layered  $\text{Al}(\text{OH})_3$

## 4.2 Calculation Methods

We performed first-principles calculation using the generalized-gradient approximation of Perdew-Burke-Ernzerhof (GGA, PBE) exchange-correlation functional implemented in VASP code with plane wave basis. Pseudopotential was made by projected augmented wave (PAW) method. The kinetic energy cutoff was set to 500eV for electronic band calculation and 800eV for relaxation of unitcells.  $9 \times 9 \times 4$  Monkhorst pack k-point grid is used for

bulk and  $9 \times 9 \times 1$  is used for single layer calculation.

## 4.3 Results and Discussion

### 4.3.1 Crystal structure of aluminum Hydroxide

There are a lot of materials constituted by Aluminum, Oxygen, and Hydrogen atoms with various compositions. Among those materials, only several kinds of materials have layered structure. We suggest the  $\alpha$ ,  $\gamma$ -phase  $\text{Al}(\text{OH})_3$  as layered material, actually which was already discovered by experiments [60–64]. However, there are not much report about their electronic band structure and its properties as layered materials with first-principles calculation. Therefore, we performed first-principles calculation for  $\text{Al}(\text{OH})_3$  focusing on their crystal structure, binding mechanism, electronic band structures, etc. Fig. 4.1 shows crystal structure of  $\alpha$ ,  $\gamma$ -phase  $\text{Al}(\text{OH})_3$ .  $\alpha$ -phase  $\text{Al}(\text{OH})_3$  is usually called as Bayerite and  $\gamma$ -phase  $\text{Al}(\text{OH})_3$  is called as Gibbsite. Both phases have a monoclinic unitcell. However, the values of  $\beta$  of monoclinic unitcell which is the angle between lattice vector  $a$  and  $c$  are both close to  $90^\circ$  degree. Therefore, the unitcell and corresponding Brillouin zone of these materials are almost close to those of orthorombic type. Layered material can be characterized as a different type of binding between intralayer and interlayer. As an example of layered material, we already know graphite or TMDs, which have strong chemical bond in single layer and weak van der Waals (vdW) interaction in-between adjacent layers. As shown in Fig. 4.1, Bayerite and Gibbsite, both are layered material having strong intralayer ionic bonding and weak interlayer binding represented as

hydrogen bonding. Bayerite and Gibbsite have a same single layer indicated by red boxes in Fig.4.1 (a) and (b) as a building block for bulk structure. In single layer  $\text{Al}(\text{OH})_3$ , As shown in a top view of single layer (Fig. 4.2 (b)), Al atoms are located as hexagonal shape with cavity at the center of hexagons. Each Al atom has six nearest oxygen atoms composing octahedron. Each octahedron shares one edge with adjacent octahedron. Hydrogen atoms are connected to oxygen atoms with 1:1 ratio. Hydrogen atoms can be located along in-plane and out-of plane direction. The oxygen and hydrogen atoms with hydrogen bond in single layer is the reason of broken hexagonal symmetry. In-plane hydrogen bonds induce distortion of Al hexagon with adjusting the positions of oxygen and hydrogen atom for minimizing total energy of system. Hydrogen bonds along out-of-plane direction contribute to interlayer hydrogen bonding when layers are stacked. However, as shown in Fig. 4.1 (c) and (d), both side of single layer are distinguishable. There are six oxygen making octahedron near aluminum, there are only three oxygen in each side of single layer, and the geometry of oxygen atoms is different in each case. If you notice the direction of white triangle in Fig.4.1 (c) and (d), the difference of opposite side is well represented. Therefore, it is possible to make distinctive phase with different stacking sequence, even though building block of bulk material is same. When we called each side of single layer  $\text{Al}(\text{OH})_3$  as A and B shown in Fig. 4.1 (c) and (d), respectively. Bayerite has a stacking sequence with AB-AB and Gibbsite does with AB-BA. Due to different stacking, two phase can be distinguished and the optimized unitcell have different geometry of hydrogen bonds and lattice constant of the unitcell, especially the lattice constant  $c$  closely related to

interlayer distance, and the angle  $\beta$  of monoclinic unitcell. Details of optimized structure for Bayerite and Gibbsite and single layer are in Table. 1. As shown in Table. 1, Bayerite and Gibbsite have similar inplane lattice constant value. Single layer  $\text{Al}(\text{OH})_3$  show a about 1% larger value of inplane lattice constant a, b than bulk case. However, in case of single layer, we cannot define lattice constant c and volume of unitcell. Lattice constant c of Gibbsite is larger than that of Bayerite, which comes from different hydrogen bonding structure between adjacent layers. The adjacency of same side of single layer make the hydrogen bond closer to perpendicular direction with respect to Bayerite case, resulting in larger optimized value of lattice constant c closely related to interlayer distance.

We can verify that Bayerite and Gibbsite, by total energy calculation using DFT, both are considered energetically as layered structure by comparing cohesive energy within single layer and interlayer binding energy among single layers, which means additional energy to break intralayer binding and interlayer binding, respectively. Starting from a set of isolated atoms, we obtained cohesive energy of single layer is 4.65eV/atom and exfoliation energy of single layer  $\text{Al}(\text{OH})_3$  from Bayerite and Gibbsite are 77.5 and 81.1 meV/atom, which can be converted as 43.3 and 45.3meV/Å<sup>2</sup> considering number of atoms in unit area. From the calculated value of cohesive energy and exfoliation energy, we could know Bayerite and Gibbsite have stronger intralayer binding than interlayer binding. and interlayer binding containing hydrogen bonding has much stronger binding strength than the cases with vdW interaction, for example, 22meV/Å<sup>2</sup> of graphite and

Table 1: Unitcell information for layered structure and single layer of  $\text{Al}(\text{OH})_3$

	Bayerite	Gibbsite	Single Layer
a(Å)	5.03	5.03	5.08
b(Å)	8.66	8.65	8.68
c(Å)	9.12	9.53	-
$\beta(^{\circ})$	90.45	92.34	-
V(Å <sup>3</sup> )	397.27	414.50	-

28meV/Å<sup>2</sup> of h-BN with same exfoliation energy calculation scheme(ref jonghyun).

### 4.3.2 Electronic band structure of Gibbsite, Bayerite & Single Layer

We obtain electronic band structures of Bayerite, Gibbsite and single layer using optimized lattice parameters in Table. 1. As shown in Fig. 4.2, Bayerite and Gibbsite are both insulator with large band gap as much as 5.54 and 5.27eV, respectively. Both are in an ultraviolet photon energy scale. As shown in PDOS analysis for both bulk materials (Fig. 4.2), valence bands are constituted by mainly oxygen orbital and conduction bands are constituted by oxygen orbitals with a little more Al, H atomic orbitals, which indirectly means the strong ionic character of intralayer bonding having large electron transfer to oxygen atoms. In detail, valence bands contain mostly oxygen p-orbital. In contrast, conduction bands have larger portion of oxygen s-orbital than valence bands. Even though Bayerite and Gibbsite have similar composition of conduction and valence band, they have different gap style. Bayerite have conduction band edge and valence band edge at  $\Gamma$ -point

at the same time, which means direct gap. However, in case of Gibbsite, valence band edge is at E-point in k-space of monoclinic unitcell, resulting in indirect gap. We also obtain an electronic band structure of single layer of  $\text{Al}(\text{OH})_3$  shown in Fig. 4.3 (c). The band gap of single layer is 4.46 eV and it is a decreased value around 1eV compared to bulk band gap. We notice at this point and try to find the reason of gap decreasing when single layer is exfoliated. We compare the electronic band structure of single layer  $\text{Al}(\text{OH})_3$  with bulk band by projection of bulk-spectrum onto 2D-BZ of single layer as shown in Fig. 4.3 (c). By comparing two band structures, we found specific bands in single layer case that are slightly less dispersive than 2D-projected bulk spectrum and located at the bottom of conduction band outside of the bulk band spectrum. We think that they are a kind of surface state when single layer is exfoliated from bulk. Additionally, we also performed electronic band structure calculation for multi-layered structure with increasing number of layer with Bayerite and Gibbsite stacking sequence, respectively. As we expected, in every calculation result, we found the states similar to characteristic states found in single-layered case. To ensure that they are surface state, we plot the real space charge density with Bloch wavefunction at conduction band edge for single-layered and multi-layered cases. In both cases, electrons in Bloch states at conduction band edge are localized near surface atoms in outermost layers and even outside of the layers as shown in Fig. 4.4 (a) and (b). To ensure surface localization, we also project the Bloch wavefunctions of multi-layered band structure to atomic orbitals located in surface and bulk region, respectively. As shown in Fig. 4.4 (c), Bloch states at bottom of conduction band in multi-layered

structure calculation are highly localized in surface region, having large portion of atomic orbitals near surface atoms located at outermost layers. These characteristic surface states and steeper dispersion of conduction bands than that of valence bands are understood as the result of strong hybridization between atomic orbital and vacuum states near surfaces. In a PDOS analysis for bulk electronic band structures represented in Fig. 4.2, there are sizable difference between total density of states(TDOS) and sum of PDOS over all of the composing atoms, which is the proof for large portion of plane waves uncounted in atomic orbital projection. Additionally, general dispersion and bandwidth of conduction band are quite similar to nearly free electron-like bands. Nearly free electron-like bands are found in 2D material calculations with large vacuum region in the unitcell, which show the dispersion character similar to the curves ruled by the  $E-k$  relation  $E = \hbar^2 k^2 / 2m$  except for zone boundaries. These states are usually in conduction bands, whose number of states increases when vacuum region of unitcell is increased.  $\text{Al}(\text{OH})_3$  also has 5.3 eV work function when surface is created. This work function value is comparable to bulk band gap, which results in strong hybridization between conduction band and vacuum states. Abovementioned strong hybridization can explain much steeper dispersion of conduction bands composed of oxygen 2s orbitals than valence bands composed of generally more dispersive 2p orbital. Strong hybridization between materials with vacuum also can describe the emergence of characteristic surface states as intensified hybridization with vacuum state near surfaces when the surface exists in the system. As well as conduction band behaviors, we also observe variation of valence bands with increasing number of layer. Irrespective to number

of stacked layers, valence band edge of Gibbsite-type stacked multi-layered structures remains at S-point where E-point of bulk BZ is projected on. In contrast, valence band edge of Bayerite-type multi-layered structures moves from S-point to  $\Gamma$ -point even from bilayer case showing increase of highest band energy at  $\Gamma$ . Except for characteristic surface states, the number of other bands increase with increasing number of stacked layers and those bands evolve to more similar shapes with bulk projection results.

### **4.3.3 Alkali-halide Intercalated $\text{Al}(\text{OH})_3$**

Many researchers have emphasized potential of layered material in application, for example, in energy storage, gas absorption, catalyst and energy conversion represented by solar cell. Except for energy conversion, the advantages of layered material in these fields are not originated from characteristic electronic properties or strong binding mechanism, but structural reason. Layered materials usually have higher surface to volume ratio than 3d bulk materials and lower packing factor from large optimized distance due to weak interlayer binding. From this point of view, interlayer distance would be the most important factor for application of layered material in various fields. Therefore, tailoring crystal structure of layered material, especially related to interlayer distance has significant meaning in their application. In this context, we consider Alkali-halide intercalation as tailoring method for crystal structure of layered  $\text{Al}(\text{OH})_3$ , which actually affects to their electronic band structure

We found experimental results of alkali-halide intercalation to gibb-

site [65–67]. The crystal structure of Alkali-halide intercalated  $\text{Al}(\text{OH})_3$  is shown in Fig. 4.5. Alkali metal atoms are at the cavity site in a center of six aluminum atoms and halogen atoms are at the center of alkali-metal atoms at different layer. We obtain relaxed structures of fully doped alkali-halide intercalated into  $\alpha$  and  $\gamma$ -phase  $\text{Al}(\text{OH})_3$  and tabulate the lattice information, and their binding energy in intercalation. As shown in Table. 2, binding energies of intercalation decreases with increasing atomic radius of intercalated atoms. Relaxed structures show the trend that atomic radius of intercalation atom is closely related to lattice constant of certain direction. The size of Alkali metal (Li, Na, K) in intercalation material determines an in-plane expansion represented as lattice constant  $a$  in Table. 2. In contrast, that of halogen atoms (Cl, Br, I) does an interlayer distance, which can be understood from lattice constant  $c$  in Table. 2. However, lattice constant  $c$  is also affected by Alkali metal atoms of intercalated material. When atomic radius of Alkali-metal increases, it gives smaller lattice constant  $c$ , which is the result of optimized distance due to interaction between alkali metal and halogen atoms. In Li-halide intercalated system, the calculation results show similar trend to experimental results [66]. Intercalated atoms contribute to breaking of intralayer and interlayer hydrogen bonds and obtaining hexagonal symmetry with adjusting oxygen and hydrogen atoms. We observe the alignment of hydrogen atoms heading for intercalated atoms. So, optimized intercalated structures seem having higher symmetry than the case of Gibbsite and Bayerite having much less total energy variation depending on hydrogen direction. As a result of geometry optimization including cell relaxation, intercalated structures changes from monoclinic unitcell to

Table 2: Unitcell information and binding energy of alkali-halide intercalated  $\text{Al}(\text{OH})_3$

Alkali-Halide intercalated $\text{Al}(\text{OH})_3$			
Bayerite/Gibbsite	$\text{Li}[\text{Al}_2(\text{OH})_6]\text{Cl}$	$\text{Li}[\text{Al}_2(\text{OH})_6]\text{Br}$	$\text{Li}[\text{Al}_2(\text{OH})_6]\text{I}$
a(Å)	5.12/5.12	5.12/5.13	5.12/5.12
c(Å)	13.90/14.21	14.58/14.62	15.02/15.52
V(Å <sup>3</sup> )	315.72/322.03	331.05/332.75	341.44/351.93
$\Delta\text{BE}(\text{eV})$	-8.80/-8.64	-8.39/-8.23	-7.81/-7.80
Bayerite/Gibbsite	$\text{Na}[\text{Al}_2(\text{OH})_6]\text{Cl}$	$\text{Na}[\text{Al}_2(\text{OH})_6]\text{Br}$	$\text{Na}[\text{Al}_2(\text{OH})_6]\text{I}$
a(Å)	5.28/5.28	5.28/5.28	5.28/5.28
c(Å)	13.46/13.64	13.94/14.34	14.69/15.17
V(Å <sup>3</sup> )	324.71/329.84	336.86/346.67	355.22/366.03
$\Delta\text{BE}$	-7.13/-6.95	-6.62/-6.50	-6.06/-6.00
Bayerite/Gibbsite	$\text{K}[\text{Al}_2(\text{OH})_6]\text{Cl}$	$\text{K}[\text{Al}_2(\text{OH})_6]\text{Br}$	$\text{K}[\text{Al}_2(\text{OH})_6]\text{I}$
a(Å)	5.48/5.48	5.47/5.48	5.47/5.48
c(Å)	12.90/13.04	13.58/13.93	14.35/14.75
V(Å <sup>3</sup> )	335.00/339.15	351.89/362.48	372.15/384.08
$\Delta\text{BE}$	-4.22/-4.01	-3.74/-3.59	-3.21/-3.14

hexagonal unitcell shown in Fig. 4.5

#### 4.3.4 Electronic band structure of alkali-halide intercalated $\text{Al}(\text{OH})_3$

Intercalation affects not only to crystal structure of layered materials, but also to their electronic band structure. We obtain their electronic band structure for each cases mentioned in Table. 2. They shows minor variations usually observed in layered materials. Alkali-atoms contribute to conduction bands and deep level of valence bands with small amount seen from the results of PDOS analysis. However, the contribution from halogen atoms appears at conduction and valence, both bands near Fermi-energy. In conduction bands, as a result of structure symmetrization originated from the

interaction among halogen p-orbital and adjacent atomic orbitals, there are strongly hybridized Bloch states at bottom of conduction band region, showing sizable halogen p-orbital portion with oxygen, aluminum, and hydrogen atomic orbitals. There are characteristic changes induced by halogen atom intercalation in valence band region also. Fig. 4.6 (a) shows the electronic band structures and PDOS with LiCl(Br, I) intercalation and Fig. 4.6 (b) shows the result for the projection of Bloch wavefunctions to oxygen and halogen p-orbital. The results of PDOS analysis show that valence band are mainly composed of oxygen p-orbital and halogen p-orbitals. When atomic number of halogen atom increases, the contribution of halogen atom to the valence band near Fermi-energy is drastically increased, and it is understood in molecular-orbital point of view. The hybridization between oxygen p-orbital and halogen p-orbital decreases due to the increasing on-site energy of Cl 3p, Br 4p, and I 5p-orbitals with respect to fixed on-site energy value of oxygen p-orbitals, which induces less hybridization.

## 4.4 Summary

We have investigated Aluminum hydroxide in a view of layered material. Bayerite and Gibbsite, both bulk phase are composed of same building block, single layer  $\text{Al}(\text{OH})_3$ , however, with different stacking sequence. Adjacent layers are bound by hydrogen bonds, which give stronger interlayer binding energy compared to that of typical layered material with vdW-interaction as interlayer binding mechanism. From the single-layered and multi-layered structure calculation, we found that exfoliation or creation of

surface induce emergence of surface localized states at the bottom of conduction band, which is the main reason for decrease of band gap. These characteristics in band structure come from the strong hybridization between materials and vacuum due to similarity of band gap to the work function of given materials. Finally, we suggest Alkali-halide intercalation for engineering method affecting not only crystal structure, but also electronic band structure. As aforementioned results show, there are also interesting phenomena in hydrogen bonded layered materials like as vdW-interaction layered materials. We also found various physical properties with tailoring crystal structures of layered material. Starting with this study on layered structure  $\text{Al}(\text{OH})_3$  in this paper, I expect that there will be a lot of the increasing interest in layered materials with a hydrogen bonding as interlayer binding mechanism.

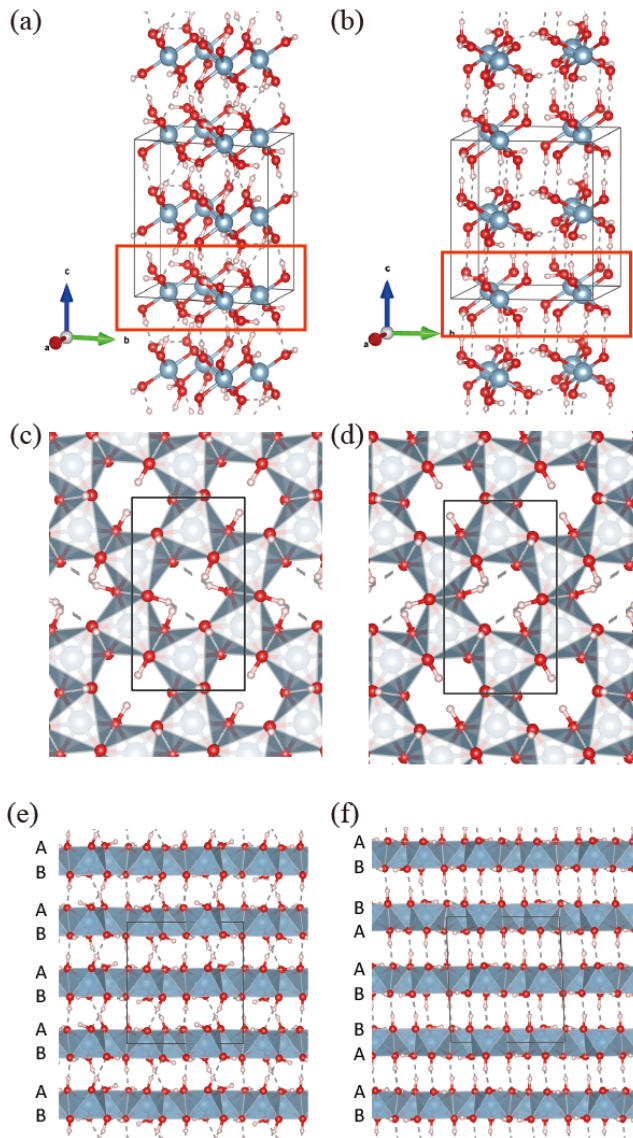


Figure 4.1: Crystal structure of (a) Bayerite and (b) Gibbsite. two phases have the same building block for layered structure. the same single layer is indicated in red rectangle in each Bayerite and Gibbsite crystal structure. (c),(d) Opposite sides of single layer  $A(OH)_3$  (A, B side). Drawing octahedron show different direction of oxygen around aluminum at each side. (d),(e) Stacking sequence of Bayerite and Gibbsite. Bayerite is stacked by AB-AB and Gibbsite is stacked by AB-BA sequence.

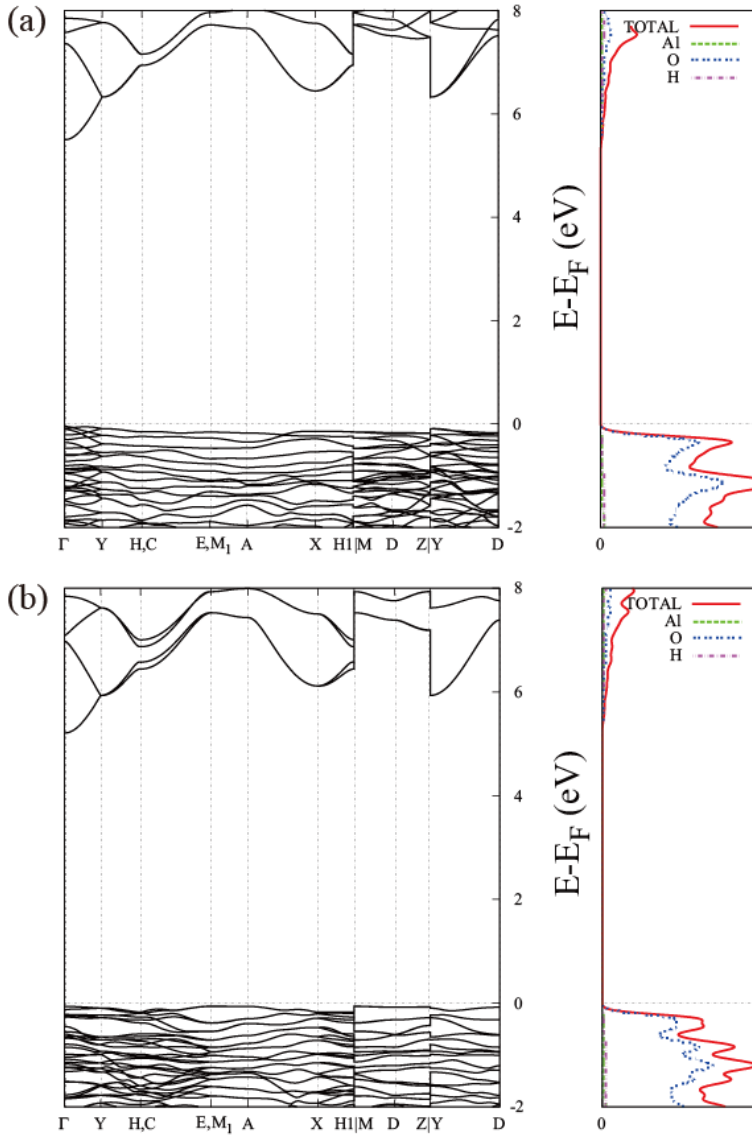


Figure 4.2: Electronic band structure and their projected density of states.(PDOS) of (a) Bayerite and (b) Gibbsite. Bayerite is a direct gap insulator with 5.54eV and Gibbsite is a indirect gap insulator with 5.27eV. In both materials, valence bands are mostly composed of oxygen p-orbital. Conduction bands contain oxygen s,p, aluminum s, hydrogen s, p-orbitals.

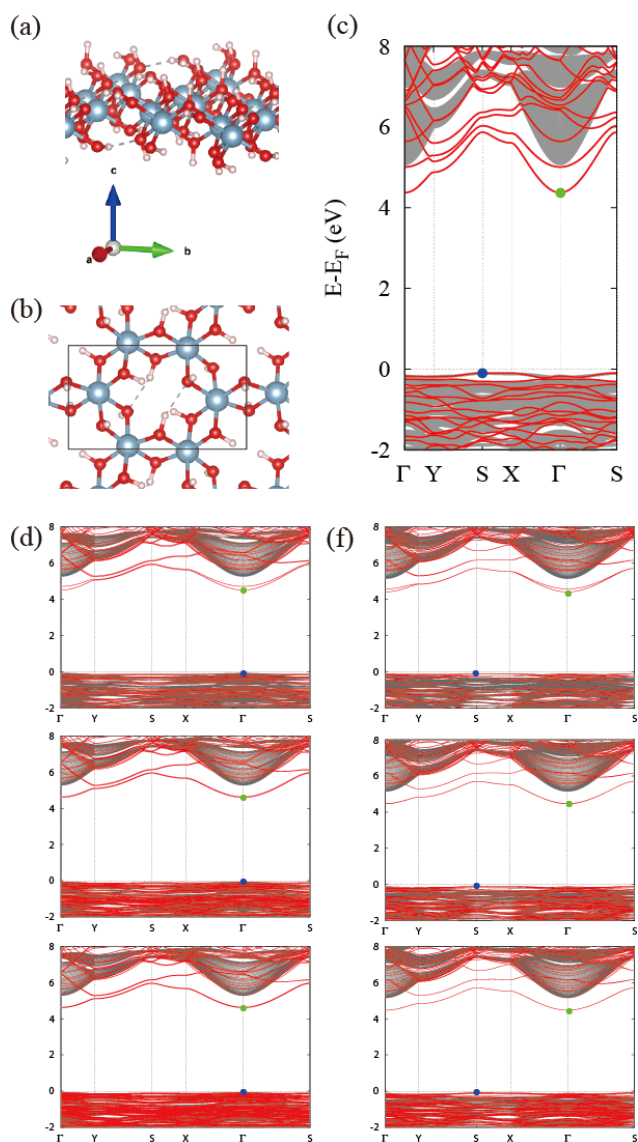


Figure 4.3: (a) Crystal structure of single layer  $\text{Al}(\text{OH})_3$ . (b) Top view of single layer  $\text{Al}(\text{OH})_3$ . (c) electronic band structure of single layer  $\text{Al}(\text{OH})_3$ (red) with bulk spectrum(grey) projected to two-dimensional Brillouin zone of single layer. (d) electronic band structure of bayerite-type 2, 4, 6-layered slab geometry with 2D-projected bulk spectrum (e) electronic band structure of gibbsite-type 2, 4, 6-layered slab geometry with 2D-projected bulk spectrum.

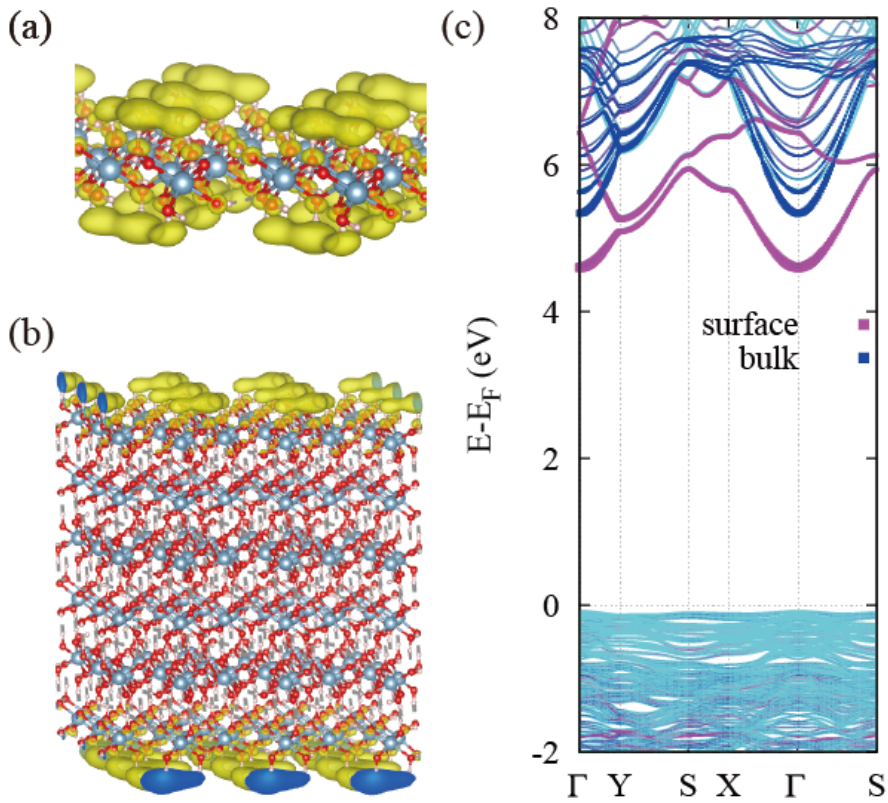


Figure 4.4: (a) Charge density of conduction band edge of single-layered  $\text{Al}(\text{OH})_3$ . (b) Charge density of conduction band edge of multi-layered  $\text{Al}(\text{OH})_3$ . In both cases, electrons are localized near surface atoms in outermost layers or even outside of the layer. (c) Localization of surface state in slab structure calculation based on PDOS analysis. surface region is defined as most upper and lower layer.

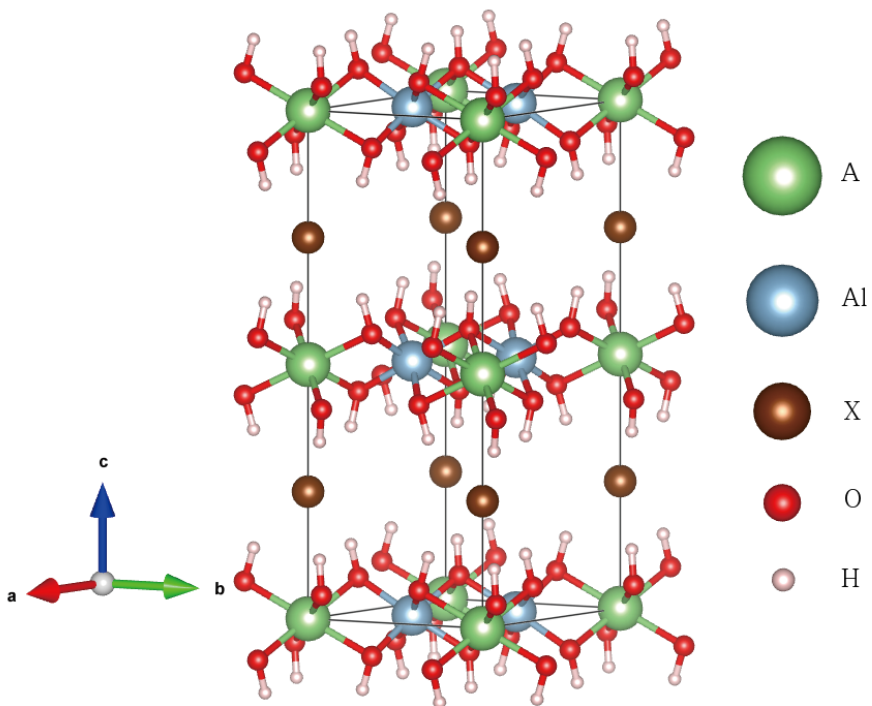


Figure 4.5: Crystal structure of Alkali-halide intercalated  $\text{Al}(\text{OH})_3$ . Alkali metal is located at the center of Al hexagon and halogen atom is at the center of Alkali metals. Lattice constants are determined by atomic radius of intercalated atoms.

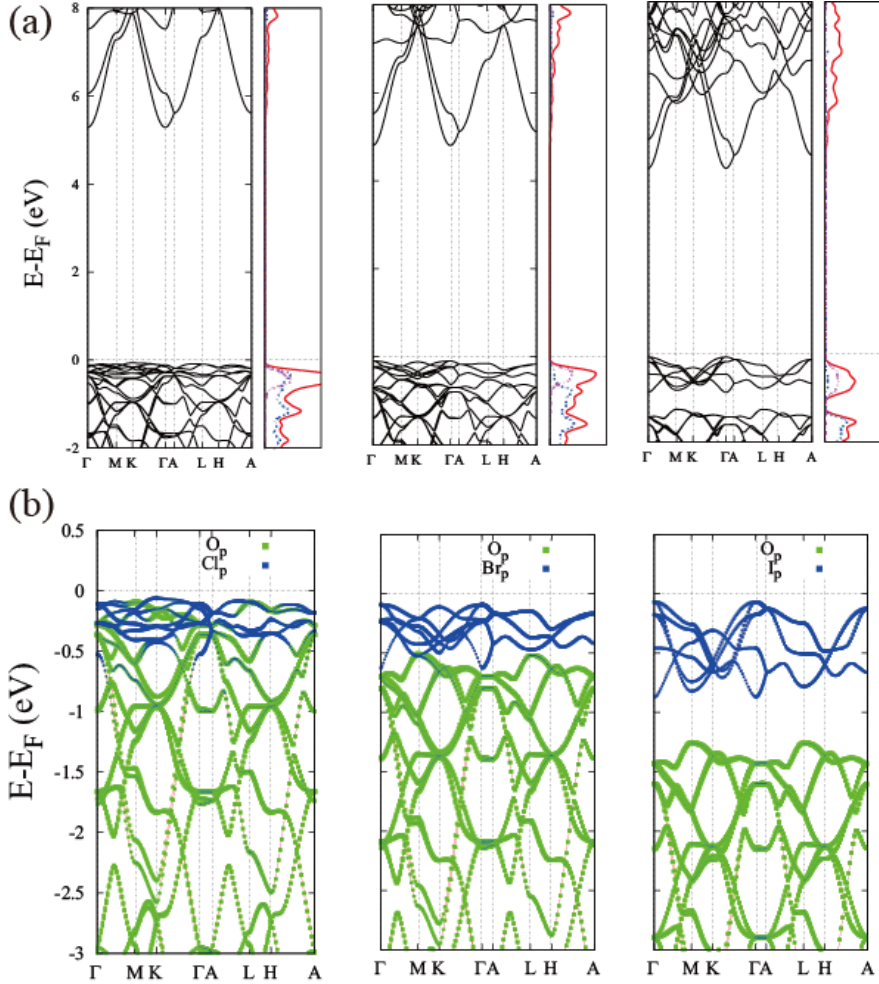


Figure 4.6: (a) Electronic band structure and PDOS for Li-halide intercalated  $\text{Al}(\text{OH})_3$  (Cl, Br, I case from the left to right panel). (b) relative ratio of oxygen p and halide p orbital (Cl, Br, I case from the left to right panel) in valence bands. the size of dot is proportional to the occupation of atomic orbital in Bloch state.



# Chapter 5

## Summary

In this thesis, I studied on two subjects related to 2d materials using first-principles calculation. In the first subject, I present atomistic models understanding the motions of GBs observed during TEM experiments and obtaining quantitative results from DFT calculation. Based on first-principles calculations, I analyze the process of structure transformations near GBs. I found that GBs can migrate through series of Stone-Wales (SW)-type transformations, Energy barrier for the SW-type transformation is greatly reduced to 7.23 eV due to the presence of GBs. which can occur much more easily near the GBs than in pristine graphene. I also show that GBs can drive the evaporation of a carbon dimer having a greatly reduced energy barrier due to the structural reconstruction near the GBs, which is lower than that in pristine graphene and separated into two smaller energy barriers. I also energetically verified that these structural transformations are due not to thermodynamics, but to energy inserted from the irradiated electron beams. Our findings contribute to the understanding of GB motion under electron beam irradiation, and thus, they may guide experimental efforts for controlling GBs in CVD graphene and for tailoring the material properties of CVD graphene.

In the second subject, I have investigated Aluminum hydroxide in a view of layered material. Two bulk phases, called Bayerite and Gibbsite, are com-

posed of the same building block, single layer  $\text{Al}(\text{OH})_3$ . In both phases, adjacent layers are bound by hydrogen bonds, which give stronger interlayer binding energy compared to that of typical layered material with vdW-interaction as interlayer binding mechanism. However, due to their different stacking sequence, they show different size and directness of band gap. From the single-layered and multi-layered structure calculation, I found that exfoliation or creation of surface induce emergence of surface localized states at the bottom of conduction band, which is the main reason for decrease of band gap. I found that these characteristics in band structure come from the strong hybridization between materials and vacuum due to similarity of band gap to the work function of given materials. Finally, I suggest Alkali-halide intercalation for engineering method affecting not only crystal structure, but also electronic band structure.

# Bibliography

- [1] K. S. Novoselov, A. K. Geim, S. V. Morozov, D. Jiang, Y. Zhang, S. V. Dubonos, I. V. Grigorieva, and A. A. Firsov, “Electric field effect in atomically thin carbon films,” *Science*, vol. 306, no. 5696, pp. 666–669, 2004.
- [2] C. Berger, Z. Song, T. Li, X. Li, A. Y. Ogbazghi, R. Feng, Z. Dai, A. N. Marchenkov, E. H. Conrad, P. N. First, and W. A. de Heer, “Ultra-thin epitaxial graphite: 2d electron gas properties and a route toward graphene-based nanoelectronics,” *The Journal of Physical Chemistry B*, vol. 108, no. 52, pp. 19912–19916, 2004.
- [3] C. Berger, Z. Song, X. Li, X. Wu, N. Brown, C. Naud, D. Mayou, T. Li, J. Hass, A. N. Marchenkov, E. H. Conrad, P. N. First, and W. A. de Heer, “Electronic confinement and coherence in patterned epitaxial graphene,” *Science*, vol. 312, no. 5777, pp. 1191–1196, 2006.
- [4] K. K. Kim, A. Reina, Y. Shi, H. Park, L.-J. Li, Y. H. Lee, and J. Kong, “Enhancing the conductivity of transparent graphene films via doping,” *Nanotechnology*, vol. 21, no. 28, p. 285205, 2010.
- [5] X. Li, W. Cai, J. An, S. Kim, J. Nah, D. Yang, R. Piner, A. Velamakanni, I. Jung, E. Tutuc, S. K. Banerjee, L. Colombo, and R. S. Ruoff, “Large-area synthesis of high-quality and uniform graphene films on copper foils,” *Science*, vol. 324, no. 5932, pp. 1312–1314, 2009.
- [6] X. Blase, A. Rubio, S. G. Louie, and M. L. Cohen, “Quasiparticle band structure of bulk hexagonal boron nitride and related systems,” *Phys. Rev. B*, vol. 51, pp. 6868–6875, Mar 1995.
- [7] H. Henck, D. Pierucci, G. Fugallo, J. Avila, G. Cassabois, Y. J. Dappe, M. G. Silly, C. Chen, B. Gil, M. Gatti, F. Sottile, F. Sirotti, M. C.

- Asensio, and A. Ouerghi, “Direct observation of the band structure in bulk hexagonal boron nitride,” *Phys. Rev. B*, vol. 95, p. 085410, Feb 2017.
- [8] E. Tegeler, N. Kosuch, G. Wiech, and A. Faessler, “On the electronic structure of hexagonal boron nitride,” *physica status solidi (b)*, vol. 91, no. 1, pp. 223–231, 1979.
- [9] R. S. Singh, R. Y. Tay, W. L. Chow, S. H. Tsang, G. Mallick, and E. H. T. Teo, “Band gap effects of hexagonal boron nitride using oxygen plasma,” *Applied Physics Letters*, vol. 104, no. 16, p. 163101, 2014.
- [10] N. Ooi, A. Rairkar, L. Lindsley, and J. B. Adams, “Electronic structure and bonding in hexagonal boron nitride,” *Journal of Physics: Condensed Matter*, vol. 18, no. 1, p. 97, 2006.
- [11] G.-B. Liu, D. Xiao, Y. Yao, X. Xu, and W. Yao, “Electronic structures and theoretical modelling of two-dimensional group-vib transition metal dichalcogenides,” *Chem. Soc. Rev.*, vol. 44, pp. 2643–2663, 2015.
- [12] J. Kang, S. Tongay, J. Li, and J. Wu, “Monolayer semiconducting transition metal dichalcogenide alloys: Stability and band bowing,” *Journal of Applied Physics*, vol. 113, no. 14, p. 143703, 2013.
- [13] F. A. Rasmussen and K. S. Thygesen, “Computational 2d materials database: Electronic structure of transition-metal dichalcogenides and oxides,” *The Journal of Physical Chemistry C*, vol. 119, no. 23, pp. 13169–13183, 2015.
- [14] P. Y. Huang, C. S. Ruiz-Vargas, A. M. van der Zande, W. S. Whitney, M. P. Levendorf, J. W. Kevek, S. Garg, J. S. Alden, C. J. Hustedt, Y. Zhu, J. Park, P. L. McEuen, and D. A. Muller, “Grains and grain boundaries in single-layer graphene atomic patchwork quilts,” *Nature*, vol. 469, p. 389, 2011.

- [15] P. Nemes-Incze, K. J. Yoo, L. Tapasztó, G. Dobrik, J. Lábár, Z. E. Horváth, C. Hwang, and L. P. Biró, “Revealing the grain structure of graphene grown by chemical vapor deposition,” *Applied Physics Letters*, vol. 99, no. 2, p. 023104, 2011.
- [16] O. V. Yazyev and S. G. Louie, “Electronic transport in polycrystalline graphene,” *Nature Materials*, vol. 9, p. 806, 2010.
- [17] O. V. Yazyev and S. G. Louie, “Topological defects in graphene: Dislocations and grain boundaries,” *Phys. Rev. B*, vol. 81, p. 195420, May 2010.
- [18] A. W. Tsen, L. Brown, M. P. Levendorf, F. Ghahari, P. Y. Huang, R. W. Havener, C. S. Ruiz-Vargas, D. A. Muller, P. Kim, and J. Park, “Tailoring electrical transport across grain boundaries in polycrystalline graphene,” *Science*, vol. 336, no. 6085, pp. 1143–1146, 2012.
- [19] S. Malola, H. Häkkinen, and P. Koskinen, “Structural, chemical, and dynamical trends in graphene grain boundaries,” *Phys. Rev. B*, vol. 81, p. 165447, Apr 2010.
- [20] B. Westenfelder, J. C. Meyer, J. Biskupek, S. Kurasch, F. Scholz, C. E. Krill, and U. Kaiser, “Transformations of carbon adsorbates on graphene substrates under extreme heat,” *Nano Letters*, vol. 11, no. 12, pp. 5123–5127, 2011. PMID: 22022781.
- [21] L. P. Biró and P. Lambin, “Grain boundaries in graphene grown by chemical vapor deposition,” *New Journal of Physics*, vol. 15, no. 3, p. 035024, 2013.
- [22] Q. Yu, L. A. Jauregui, W. Wu, R. Colby, J. Tian, Z. Su, H. Cao, Z. Liu, D. Pandey, D. Wei, T. F. Chung, P. Peng, N. P. Guisinger, E. A. Stach, J. Bao, S.-S. Pei, and Y. P. Chen, “Control and characterization of individual grains and grain boundaries in graphene grown by chemical vapour deposition,” *Nature Materials*, vol. 10, p. 443, 2011.

- [23] B. Song, G. F. Schneider, Q. Xu, G. Pandraud, C. Dekker, and H. Zandbergen, “Atomic-scale electron-beam sculpting of near-defect-free graphene nanostructures,” *Nano Letters*, vol. 11, no. 6, pp. 2247–2250, 2011. PMID: 21604710.
- [24] S. Kurasch, J. Kotakoski, O. Lehtinen, V. Skákalová, J. Smet, C. E. Krill, A. V. Krasheninnikov, and U. Kaiser, “Atom-by-atom observation of grain boundary migration in graphene,” *Nano Letters*, vol. 12, no. 6, pp. 3168–3173, 2012. PMID: 22554303.
- [25] P.-C. Yeh, W. Jin, N. Zaki, D. Zhang, J. T. Liou, J. T. Sadowski, A. Al-Mahboob, J. I. Dadap, I. P. Herman, P. Sutter, and R. M. Osgood, “Layer-dependent electronic structure of an atomically heavy two-dimensional dichalcogenide,” *Phys. Rev. B*, vol. 91, p. 041407, Jan 2015.
- [26] E. Pomerantseva and Y. Gogotsi, “Two-dimensional heterostructures for energy storage,” *Nature Energy*, vol. 2, p. 17089, 2017.
- [27] P. Kumar, H. Abuhimd, W. Wahyudi, M. Li, J. Ming, and L.-J. Li, “Review?two-dimensional layered materials for energy storage applications,” *ECS Journal of Solid State Science and Technology*, vol. 5, no. 11, pp. Q3021–Q3025, 2016.
- [28] A. Kumar and Q. Xu, “Two-dimensional layered materials as catalyst supports,” *ChemNanoMat*, vol. 4, no. 1, pp. 28–40, 2018.
- [29] P. Hohenberg and W. Kohn, “Inhomogeneous electron gas,” *Phys. Rev.*, vol. 136, pp. B864–B871, Nov 1964.
- [30] W. Kohn and L. J. Sham, “Self-consistent equations including exchange and correlation effects,” *Phys. Rev.*, vol. 140, pp. A1133–A1138, Nov 1965.
- [31] D. M. Ceperley and B. J. Alder, “Ground state of the electron gas by a stochastic method,” *Phys. Rev. Lett.*, vol. 45, pp. 566–569, Aug 1980.

- [32] L. Hedin and S. O. Lundqvist, *Effects of Electron-Electron and Electron-Phonon Interactions on the One-Electron States of Solids*, vol. 23 of *Solid State Physics*, pp. 1–181. Academic Press, 1969.
- [33] J. P. Perdew and A. Zunger, “Self-interaction correction to density-functional approximations for many-electron systems,” *Phys. Rev. B*, vol. 23, pp. 5048–5079, May 1981.
- [34] S. H. Vosko, L. Wilk, and M. Nusair, “Accurate spin-dependent electron liquid correlation energies for local spin density calculations: a critical analysis,” *Canadian Journal of Physics*, vol. 58, no. 8, pp. 1200–1211, 1980.
- [35] J. P. Perdew, K. Burke, and M. Ernzerhof, “Generalized gradient approximation made simple,” *Phys. Rev. Lett.*, vol. 77, pp. 3865–3868, Oct 1996.
- [36] C. Lee, X. Wei, J. W. Kysar, and J. Hone, “Measurement of the elastic properties and intrinsic strength of monolayer graphene,” *Science*, vol. 321, no. 5887, pp. 385–388, 2008.
- [37] I. W. Frank, D. M. Tanenbaum, A. M. van der Zande, and P. L. McEuen, “Mechanical properties of suspended graphene sheets,” *Journal of Vacuum Science & Technology B: Microelectronics and Nanometer Structures Processing, Measurement, and Phenomena*, vol. 25, no. 6, pp. 2558–2561, 2007.
- [38] R. R. Nair, P. Blake, A. N. Grigorenko, K. S. Novoselov, T. J. Booth, T. Stauber, N. M. R. Peres, and A. K. Geim, “Fine structure constant defines visual transparency of graphene,” *Science*, vol. 320, no. 5881, pp. 1308–1308, 2008.
- [39] A. B. Kuzmenko, E. van Heumen, F. Carbone, and D. van der Marel, “Universal optical conductance of graphite,” *Phys. Rev. Lett.*, vol. 100, p. 117401, Mar 2008.

- [40] X. Li, C. W. Magnuson, A. Venugopal, R. M. Tromp, J. B. Hannon, E. M. Vogel, L. Colombo, and R. S. Ruoff, “Large-area graphene single crystals grown by low-pressure chemical vapor deposition of methane on copper,” *Journal of the American Chemical Society*, vol. 133, no. 9, pp. 2816–2819, 2011. PMID: 21309560.
- [41] A. Reina, X. Jia, J. Ho, D. Nezich, H. Son, V. Bulovic, M. Dresselhaus, and J. Kong *Nano Lett.*, vol. 8, pp. 30–35, 2008. cited By 2.
- [42] D. Wei, Y. Liu, Y. Wang, H. Zhang, L. Huang, and G. Yu, “Synthesis of n-doped graphene by chemical vapor deposition and its electrical properties,” *Nano Letters*, vol. 9, no. 5, pp. 1752–1758, 2009. PMID: 19326921.
- [43] L. Zhao, K. Rim, H. Zhou, R. He, T. Heinz, A. Pinczuk, G. Flynn, and A. Pasupathy, “Influence of copper crystal surface on the cvd growth of large area monolayer graphene,” *Solid State Communications*, vol. 151, no. 7, pp. 509 – 513, 2011.
- [44] S. J. Chae, F. G?ne?, K. K. Kim, E. S. Kim, G. H. Han, S. M. Kim, H.-J. Shin, S.-M. Yoon, J.-Y. Choi, M. H. Park, C. W. Yang, D. Pribat, and Y. H. Lee, “Synthesis of large-area graphene layers on poly-nickel substrate by chemical vapor deposition: Wrinkle formation,” *Advanced Materials*, vol. 21, no. 22, pp. 2328–2333, 2009.
- [45] H. Zhou, W. J. Yu, L. Liu, R. Cheng, Y. Chen, X. Huang, Y. Liu, Y. Wang, Y. Huang, and X. Duan, “Chemical vapour deposition growth of large single crystals of monolayer and bilayer graphene,” *Nature Communications*, vol. 4, p. 2096, 2013.
- [46] J. P. Perdew, K. Burke, and M. Ernzerhof, “Generalized gradient approximation made simple [phys. rev. lett. 77, 3865 (1996)],” *Phys. Rev. Lett.*, vol. 78, pp. 1396–1396, Feb 1997.
- [47] P. E. Blöchl, “Projector augmented-wave method,” *Phys. Rev. B*, vol. 50, pp. 17953–17979, Dec 1994.

- [48] G. Kresse and J. Furthmüller, “Efficiency of ab-initio total energy calculations for metals and semiconductors using a plane-wave basis set,” *Computational Materials Science*, vol. 6, no. 1, pp. 15 – 50, 1996.
- [49] J. Kotakoski, J. C. Meyer, S. Kurasch, D. Santos-Cottin, U. Kaiser, and A. V. Krasheninnikov, “Stone-wales-type transformations in carbon nanostructures driven by electron irradiation,” *Phys. Rev. B*, vol. 83, p. 245420, Jun 2011.
- [50] H. F. Bettinger, B. I. Yakobson, and G. E. Scuseria, “Scratching the surface of buckminsterfullerene: the barriers for stone-wales transformation through symmetric and asymmetric transition states,” *Journal of the American Chemical Society*, vol. 125, no. 18, pp. 5572–5580, 2003. PMID: 12720471.
- [51] G.-D. Lee, C. Z. Wang, E. Yoon, N.-M. Hwang, D.-Y. Kim, and K. M. Ho, “Diffusion, coalescence, and reconstruction of vacancy defects in graphene layers,” *Phys. Rev. Lett.*, vol. 95, p. 205501, Nov 2005.
- [52] K. Kim, S. Coh, C. Kisielowski, M. F. Crommie, S. G. Louie, M. L. Cohen, and A. Zettl, “Atomically perfect torn graphene edges and their reversible reconstruction,” *Nature Communications*, vol. 4, p. 2723, 2013.
- [53] L. Li, S. Reich, and J. Robertson, “Defect energies of graphite: Density-functional calculations,” *Phys. Rev. B*, vol. 72, p. 184109, Nov 2005.
- [54] F. Banhart, J. Kotakoski, and A. Krasheninnikov *Acs Nano*, vol. 5, p. 26, 2010. cited By 1.
- [55] G.-D. Lee, C. Z. Wang, E. Yoon, N.-M. Hwang, and K. M. Ho, “Reconstruction and evaporation at graphene nanoribbon edges,” *Phys. Rev. B*, vol. 81, p. 195419, May 2010.

- [56] G.-D. Lee, E. Yoon, C.-Z. Wang, and K.-M. Ho, “Atomistic processes of grain boundary motion and annihilation in graphene,” *Journal of Physics: Condensed Matter*, vol. 25, no. 15, p. 155301, 2013.
- [57] F. Banhart, “Irradiation effects in carbon nanostructures,” *Reports on Progress in Physics*, vol. 62, no. 8, p. 1181, 1999.
- [58] B. W. Smith and D. E. Luzzi, “Electron irradiation effects in single wall carbon nanotubes,” *Journal of Applied Physics*, vol. 90, no. 7, pp. 3509–3515, 2001.
- [59] F. Ding, K. Jiao, Y. Lin, and B. I. Yakobson, “How evaporating carbon nanotubes retain their perfection?,” *Nano Letters*, vol. 7, no. 3, pp. 681–684, 2007. PMID: 17302460.
- [60] Y. Cesteros, P. Salagre, F. Medina, and J. E. Sueiras, “Several factors affecting faster rates of gibbsite formation,” *Chemistry of Materials*, vol. 11, no. 1, pp. 123–129, 1999.
- [61] Y. Cesteros, P. Salagre, F. Medina, and J. E. Sueiras, “A new route to the synthesis of fine-grain gibbsite,” *Chemistry of Materials*, vol. 13, no. 8, pp. 2595–2600, 2001.
- [62] S. Louaer, Y. Wang, and L. Guo, “Fast synthesis and size control of gibbsite nanoplatelets, their pseudomorphic dehydroxylation, and efficient dye adsorption,” *ACS Applied Materials & Interfaces*, vol. 5, no. 19, pp. 9648–9655, 2013. PMID: 24001258.
- [63] S. Shen, P. S. Chow, F. Chen, S. Feng, and R. B. Tan, “Synthesis of submicron gibbsite platelets by organic-free hydrothermal crystallization process,” *Journal of Crystal Growth*, vol. 292, no. 1, pp. 136 – 142, 2006.
- [64] C. Kumara, W. Ng, A. Bandara, and R. Weerasooriya, “Nanogibbsite: Synthesis and characterization,” *Journal of Colloid and Interface Science*, vol. 352, no. 2, pp. 252 – 258, 2010.

- [65] K. R. Poeppelmeier and S. J. Hwu, "Synthesis of lithium dialuminate by salt imbibition," *Inorganic Chemistry*, vol. 26, no. 20, pp. 3297–3302, 1987.
- [66] A. V. Besserguenev, A. M. Fogg, R. J. Francis, S. J. Price, D. O'Hare, V. P. Isupov, and B. P. Tolochko, "Synthesis and structure of the gibbsite intercalation compounds  $[\text{Al}_2(\text{OH})_6]_x$  X = Cl, Br, NO<sub>3</sub> and  $[\text{Al}_2(\text{OH})_6]\text{Cl}\cdot\text{H}_2\text{O}$  using synchrotron x-ray and neutron powder diffraction," *Chemistry of Materials*, vol. 9, no. 1, pp. 241–247, 1997.
- [67] A. M. Fogg and D. O'Hare, "Study of the intercalation of lithium salt in gibbsite using time-resolved in situ x-ray diffraction," *Chemistry of Materials*, vol. 11, no. 7, pp. 1771–1775, 1999.



# 국문초록

주기성은 응집 물질 혹은 고체를 이해하는 데 있어서 가장 중요한 개념이다. 이차원 물질은 3차원 공간 안에서 단지 두 독립된 방향으로만 그 주기성의 정의된다는 점에서 특별하다. 가장 대표적인 2차원 물질은 K. S. Novoselov와 A. K. Geim에 의해 실험적으로 박리된 그래핀일 것이다. 그 외에도 전이금속 다이칼코게나이드와 육각 질화 붕소와 같은 다른 단일층 물질들이 존재한다. 이러한 물질들의 여러 측면의 물리적 특성 역시 많이 보고 되었다. 이런 단일층 물질들은 층상 구조로 결합하는 것이 가능한 특성을 가지고 있는데 각 층 사이는 반데르발스 상호작용을 통해 결합한다. 반데르발스 상호작용으로부터 기인한 양한 상호작용으로 인하여 층상 구조는 그 층수, 쌓는 방식, 층상 구조를 이루는 다양한 단일층 물질의 종류 등에 따라서 다양한 물리적 성질들을 보이며, 이는 학문적, 기술적 분야의 연구자들의 관심을 끄는 이유도 작용하였다. 이러한 2차원 물질에 대한 증가하는 관심을 반영하여 나 역시 나의 학위 논문을 구성하는 두 가지 주제에 대해 고찰해보았고 그 과정에서 범밀로론함수를 통한 계산이 큰 역할을 하였다.

첫 번째 주제에서, 다결정 그래핀의 결정 경계면 근처에서 일어나는 구조 변화를 분석하였고 그 수치적 이해를 위하여 범밀도론함수를 이용하여 구조 변화에 해당하는 토탈 에너지 곡선을 얻었다. TEM 실험으로부터 관측된 대다수의 구조 변화를 만들어내는 두가지 주요한 구조 변화를 분류하였다. 첫번째는 스톤웨일즈 변환으로서, 그래핀에서도 잘 알려진 바 있다. 하지만 그 에너지 장벽의 수치를 확인해보면 일반적인 구조의 그래핀에서 일어나는 변환에 비해 감소된 값을 보이며, 이는 에너지적 측면에

서 훨씬 더 일어나기 쉬운 반응임을 확인할 수 있다. 또 다른 변환은 탄소 이합체의 증발이라고 불리우는 과정이며, 이는 평면상의 그래핀에서 두 개만큼의 탄소원자 개수를 감소시킨다. 이 역시 결정 경계면 근처에서 일어날 경우에 범밀도론 함수 계산을 통해 얻은 에너지 장벽을 통해 확인해보았을 때, 훨씬 더 일어나기 쉬워짐을 확인할 수 있었다. 또한 토탈 에너지를 최소화하는 이완된 원자 구조를 통해서 확인해보았을 때, 에너지 장벽의 감소의 이유로서의 결정 경계면 구조의 재건을 확인할 수 있었으며, 이러한 구조 변화들에서 TEM 촬영이 하는 역할을 규명할 수 있었다. 두 번째 주제에서는 층상 구조를 지닌 알루미늄 하이드록사이드에 대한 연구를 하였다. 현재까지 보고된 층상 구조를 지닌 다양한 물질들의 공통된 층간 결합 기제는 공통되게 반데르발스 상호작용이었다. 층상 구조를 지닌 알루미늄 하이드록사이드의 두가지 벌크 상으로부터 시작하여, 이를 이루는 단일층 구조와 수소 결합을 통한 층간 결합 방식에 대해 이해하려고 노력하였다. 범밀도함수론 계산을 통하여 우리는 수소 결합을 통한 층간의 결합이 단일층 구조내에 존재하는 강한 이온 결합에 비해 상대적으로 약한 결합을 이루고 있음을 밝혀내어, 에너지적으로 분석해 볼 때, 알루미늄 하이드록사이드를 층상 물질로 생각할 수 있다고 결론지었다. 그러나 수치적으로 밝혀낸 층간의 결합 에너지는 반데르발스 상호작용으로 결합된 층상 물질에서의 결합보다는 훨씬 더 강하다는 것도 확인 가능하였다. 우리는 또한 밴드 구조적 측면에서 단일 층이나 유한한 개수의 층으로 구성된 슬랩 구조에서는 전도띠의 가장 낮은 에너지 영역에 벌크 구조의 계산 결과에서는 발견되지 않는 표면 상태가 나타남을 확인할 수 있었고, 이는 이차원 구조의 전자 계산에서 밴드 갭을 감소시키는 주된 원인으로 작용함을 확인하였다. 마지막으로 우리는 층상 구조를 지닌 알루미늄 하이드록사이드의 결정 구조 뿐만 아니라 전자 구조를 목적을 가

지고 변화시킬 수 있는 수단으로서의 알칼리-할라이드 삽입을 시도하였다. 층상 물질의 응요에 있어서 가장 중요한 요소로 작용하는 층간 거리는 알칼리 금속 원자와 할로겐 원자의 종류에 동시에 영향을 받음을 밝혀내었고, 전자 구조의 측면에서는 특히나 가전자대 영역에서 알칼리-할라이드 물질의 삽입에 의하여 변할 수 있고, 이는 산소 원자와 할로겐 원자의 p-오비탈의 하이브리다이제이션으로 이해될 수 있음을 확인하였다.

**주요어 :** 이차원 물질, 결합 에너지, 토탈 에너지, 범밀도함수론

**학번 :** 2010-20359

